MECHANICAL EFFECTS ON THE ELECTRO-OPTICAL PROPERTIES
OF SILICON-CARBON NANOTUBE BASED METAMATERIALS FOR
PHOTO-ABSORBER APPLICATIONS

A THESIS SUBMITTED TO
THE BOARD OF GRADUATE PROGRAMS
OF
MIDDLE EAST TECHNICAL UNIVERSITY
NORTHERN CYPRUS CAMPUS

BY

BARIŞ ÖRDEK

IN PARTIAL FULFILLMENT OF THE REQUIREMENTS
FOR
THE
DEGREE OF MASTER OF SCIENCE
IN
THE
SUSTAINABLE ENVIRONMENT AND ENERGY SYSTEMS

SEPTEMBER 2020

Approval of the Board of Graduate Programs

_____

Prof. Dr. Gürkan Karakaş
Chairperson

I certify that this thesis satisfies all the requirements as a thesis for the degree of Master of Science.

_____

Asst. Prof. Dr. Ceren Ince Derogar
Program Coordinator

This is to certify that we have read this thesis and that in our opinion it is fully adequate, in scope and quality, as a thesis for the degree of Master of Science.

_____   _____
Prof. Dr. Cumali Sabah   Assoc. Prof. Dr. Volkan Esat
Co-Supervisor   Supervisor

Examining Committee Members

Assoc. Prof. Dr. Volkan Esat
Mechanical Engineering Prog. METU NCC   _____

Prof. Dr. Cumali Sabah
Electrical and Electronics Engineering
Prog. METU NCC   _____

Asst. Prof. Dr. Ali Berk Baştaş
Mechanical Engineering Prog. METU NCC   _____

Prof. Dr. Faruk Karadağ
Physics Prog. Çukurova University   _____

Assoc. Prof. Dr. Fatih Dikmen
Electronics Engineering Prog. GTU   _____

I hereby declare that all information in this document has been obtained and presented in accordance with academic rules and ethical conduct. I also declare that, as required by these rules and conduct, I have fully cited and referenced all material and results that are not original to this work.

Name, Last name: Barış, Ördek

Signature:

ABSTRACT

MECHANICAL EFFECTS ON THE ELECTRO-OPTICAL PROPERTIES OF SILICON-CARBON NANOTUBE BASED METAMATERIALS FOR PHOTO-ABSORBER APPLICATIONS

Ördek, Barış

M.S., Sustainable Environment and Energy Systems Program

Advisor: Assoc. Prof. Dr. Volkan Esat

Co-Advisor: Prof. Dr. Cumali Sabah

September 2020, 89 pages

The use of metamaterial (MTM) technology has been popular recently due to having extensive range of applications and being a promising field of interest. MTMs are commonly used in medical, energy, and military fields. Solar photovoltaics (PV) is one of the fields that MTMs are used in order to increase the generated energy. In this thesis, three silicon-carbon nanotube (Si-CNT) based MTM absorbers are proposed and the effect of mechanical bending stresses on the electro-optical properties of three proposed designs are investigated within the frequency range of 400 THz to 1200 THz (Visible and Ultraviolet). The proposed absorbers consist of three layers, namely: resonators, substrate, and ground plate. The resonators and ground plate are made of aluminum whereas the substrate is made of silicon-carbon nanotube composite with 5% CNT. According to the simulation results, at least 72% of solar radiation is absorbed among three absorbers. Moreover, resonance frequency shifts, dual-band frequency response, and increase in absorption rates are observed when bending deformations are applied to the proposed absorbers.

Keywords: Metamaterials, carbon nanotube, finite integration technique, resonance shifts, composite, bending moment.

ÖZ

IŞIK SOĞURAN SİLİCON-KARBON NANOTÜP TABANLI META
MALZEMELERİN ELEKTRO-OPTİK ÖZELLİKLERİ ÜZERİNDEKİ MEKANİK
ETKİLERİN İNCELENMESİ

Ördek, Barış
Yüksek Lisans, Sürdürülebilir Çevre ve Enerji Sistemleri Programı
Tez Yöneticisi: Doç. Dr. Volkan Esat
Ortak Tez Yöneticisi: Prof. Dr. Cumali Sabah
Eylül 2020, 89 sayfa

Geniş bir uygulama yelpazesine sahip olması ve gelecek vaat eden bir ilgi alanı olmasından dolayı meta malzeme teknolojisi yakın zamanın popüler araştırma alanlarından birisidir. Bu teknoloji, tıp, enerji ve askeri alanlarda yaygın olarak kullanılmaktadır. Üretilen enerji miktarını arttırmak için, meta malzemeler güneş fotovoltaikleri alanında kullanılmaktadır. Bu tezde, üç farklı silikon-karbon nanotüp bazlı meta malzemeden oluşan absorblayıcı önerilmektedir ve önerilen üç tasarımın mekanik bükülme geriliminden dolayı oluşan elektro-optik özelliklerindeki değişimler 400 THz ile 1200 THz (görünür ve ultraviole) frekans aralığında incelenmektedir. Önerilen absorblayıcılar üç katmandan oluşmaktadır: rezonatörler, substrat ve zemin plakası. Resonatörler ve zemin plakası Alüminyumdan, substrat ise silicon-karbon nanotüp kompozitinden oluşmaktadır. Kompozitin %5'i karbon nanotüpden geri kalanı ise silikondan oluşmaktadır. Simulasyon sonuçlarına göre, üç soğurucu ele alındığında, güneş ışınımının en az %72'si emilmektedir. Ayrıca, bu tezde önerilen soğuruculara bükme deformasyonları uygulandığında rezonans frekans kaymaları, çift bant frekans tepkisi ve emilim oranlarında artışlar gözlenmiştir.

Anahtar Kelimeler: Meta malzemeler, karbon nanotüp, sonlu integrasyon tekniği, rezonans kaymaları, kompozit, bükme momenti.

x

To my beloved family for their continuous support and love during my whole life.

ACKNOWLEDGEMENTS

TABLE OF CONTENTS

LIST OF TABLES

LIST OF FIGURES

FIGURES

LIST OF ABBREVIATIONS

α	Thermal expansion coefficient	1/K
ϵ	Permittivity	F/m
θ	Chiral angle	degrees
μ	Permeability	N/A^2
ν	Poisson's Ratio	-
π	Pi Number	-
ρ	density	g/cm^3
σ	Electrical conductivity	S/cm
a	Unit cell vector	-
AC	Alternating Current	A
C	Chiral vector	-
CNT	Carbon nanotube	-
d	Diameter of carbon nanotube	nm
DC	Direct current	A
DSSC	Dye-sensitized solar cell	-
DWNT	Double-walled carbon nanotube	-
E	Young's Modulus	GPa, TPa
EWT	Emitter Wrap-Through	-
GHG	Greenhouse Gas	-
K	Heat Capacity	J/K/kg
k	Thermal conductivity	W/m/K
L	Bond length	nm
m	Magnitude of unit cell vector in direction 2	-
MTM	Metamaterial	-
MWNT	Multi-walled carbon nanotube	-
n	Magnitude of unit cell vector in direction 1	-
p	Refractive index	-
PV	Photovoltaic	-
r	Reflection coefficient	-
ROM	Rule of mixtures	-
Si	Silicon element	-

SWNT	Single-walled carbon nanotube	-
V	Volume fraction	-
z	Impedance	ohm

Subscripts

1	Component of unit cell vector in direction 1	-
2	Component of unit cell vector in direction 2	-
c	Composite material	-
d	Fraction of fiber material to matrix material	-
f	Fiber material	-
h	Chiral vector	-
m	Matrix material	-
$'$	Real part of refractive index	-
$''$	Imaginary part of refractive index	-

CHAPTER 1

INTRODUCTION

In this chapter, firstly, the motivation behind this thesis is presented. General information and introduction to metamaterials (MTM) are delivered. Next, information on MTM absorbers and carbon nanotubes (CNT) is given. Then, properties and explanations on composites and rule of mixtures (ROM) are discussed. After that, mechanical deformation modes like bending are explained. Finally, the general phenomena behind the absorption theory are discussed.

1.1 Motivation

Greenhouse gas emissions (GHG) have been increasing since the industrial revolution. This is caused by the increase in the use of fossil fuels which are used to generate energy. GHG emissions have huge impacts on the environment and cause environmental problems like climate change and global warming [1]. To overcome these environmental problems, renewable energy resources are introduced as a sustainable and environmentally friendly alternative for generating energy. One of the cleanest renewable energy resources is solar energy [2]. Solar energy is converted into electricity by using photovoltaic (PV) modules [3], [4]. The efficiency of solar PV modules is relatively low when compared to other renewables [2]. One of the ways of increasing PV efficiency is integrating carbon nanotube (CNT) into PV cells. This is achieved by integrating a metamaterial absorber onto a solar PV module [5]. During the manufacturing of these CNT integrated metamaterial absorbers, some mechanical impacts occur. These mechanical impacts can occur during manufacturing, installation, or operation [4], [5]. The MTM absorber is also a part of this PV modules, and can be affected from these impacts. Thus, the main focus of this research is to investigate the effects of these mechanical impacts on Si-CNT based MTM absorbers. To do so, mechanical bending deformations are applied to three Si-CNT composite

integrated metamaterial absorbers, and these absorbers are investigated to determine the change in their electro-optical properties.

1.2 Metamaterials

Metamaterials are defined as synthetic materials with superior and uncommon properties like high conductivity, high reflectivity, and high flexibility that cannot be found in nature. In other words, they can be designed according to need [8], [9]. The metamaterial terminology is first mentioned in 1968 by V. G. Veselago who stated that a material can have both permeability and permittivity in negative state. John Pendry discovered a practical way to manufacture left-handed metamaterials that did not obey the right-hand rule, in 1999. He designed a Thin-Wire structure that has negative effective permittivity. In 2000, Smith created a new left-handed metamaterial (LHM) that can have negative permeability and permittivity simultaneously. In order to understand its uncommon properties, Smith continued to do microwave experiments on this newly invented LHM [10]. Types of metamaterials are listed as electromagnetic, chiral, terahertz, photonic, tunable, frequency selective surface-based, and nonlinear metamaterials. Electromagnetic metamaterials are used microwave and optical applications. They have a subsection in physics and electromagnetism. They are used in lenses, antenna radomes, band-pass filters, and beam steerer applications [10], [11]. Chiral metamaterials are made of planar metallic or dielectric gammadion arrays placed on a substrate [12]. Terahertz metamaterials are the combination of artificial materials that can operate at terahertz frequencies. They are still in development. They are also called passive materials because they can attain needed magnetic response due to having negative permeability values [10]. Photonic metamaterials are designed in order to operate at optical frequencies, so that, they are also called optical metamaterials [10]. Tunable metamaterials have the ability to arrange the frequency of a reflective index, randomly. Their structure can be changed in real-time, therefore, they can be rearranged during operation [10]. Frequency selective surface (FSS) based metamaterials

have static geometry and spacing in their unit cells, and they are used instead of fixed frequency metamaterials. They are used to obtain frequency response of other metamaterials. They are designed to control the reflection and transmission characteristics of incident radiation wave [10]. Nonlinear metamaterials are artificial materials with nonlinearity as the name implies. Response of electromagnetic radiation is described with permeability and permittivity of the material. They can be manufactured from nonlinear metamaterials that can change the power of incident wave [13].

Metamaterials have several applications in several fields. These fields are listed as, sensor detection, improving ultrasonic sensors, public safety, solar power management, high-frequency battlefield communications, remote aerospace, and high gain antennas. Armies use metamaterials in order to detect chemical explosives and biological contaminations. Metamaterials are used in the structure of invisible subs because they can manipulate the wavelength of sound. This technology is also used to produce soundproof rooms with perfect acoustics. Metamaterials are used to design absorbers for solar energy applications [10]. Since the properties of metamaterials can be adjusted according to the need, a perfect absorber is possible with the use of metamaterials. One of the materials that are used to create metamaterial absorber is carbon nanotube (CNT). With CNT based metamaterial absorbers, high absorption values can be achieved, so that, more energy is captured [14].

In this thesis, three Si-CNT composite integrated metamaterial absorbers will be used in order to see the effects of mechanical bending deformation on the electro-optical properties of MTM absorbers.

1.3 Metamaterial Absorbers

An MTM absorber is a device that is used to increase the absorption of a PV module. Carbon nanotube (CNT) is one of the materials that is used to create MTM absorbers. It is stated that CNT integrated MTM absorbers have high absorption rates because CNT has superior electrical and mechanical properties [15]. It is usually made of three components, a ground plate, a

substrate, and number of resonators. The ground plate prevents the light to get transmitted through the absorber. The substrate absorbs the light, and the resonators decrease the reflection within the absorber as shown in Figure 1.1. Since there is no transmission, in order to maximize the absorption, reflection must be decreased. To do so, different shapes and strips are used as resonators [14].
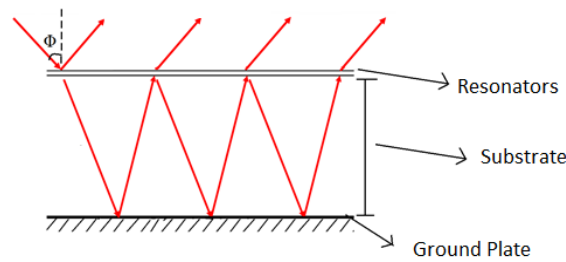
Figure 1.1 The cross section of an MTM absorber [14]

1.4 Carbon Nanotubes

Carbon nanotubes are made of rolled graphene sheets with superior properties like high conductivity, high flexibility, and high strength. They contain only hybridized carbon atoms that have hexagonal arrangement. Their geometrical structure is a seamless cylinder, and their diameter can be arranged according to the application that are going to be used [16], [17]. Carbon Nanotubes were discovered by Sumio Iijima who is a Japanese physicist, in 1991. In 1993, he discovered single-walled carbon nanotubes (SWNT). Carbon Nanotubes have great mechanical properties like 63 GPa of tensile strength and 1 TPa of Young's moduli. Not only their mechanical properties but also electrical properties are superior. They can be both semiconducting and metallic according to their diameter and structure [18], [19].

Carbon nanotubes categorized according to their geometry and number of tubes they have. The geometry of CNTs is determined by chirality of the folded graphene sheet. The chirality is defined as the geometrical way that graphene sheet is rolled [14]. The chirality determines the type of CNT. There are three

different types of CNT structures available: zigzag (n, 0), armchair (n, n), and chiral (n, m). These CNT structures are represented in Figure 1.2. The chirality depends on chiral angle and chiral vector. The chiral vector is determined from Equation 1.1. The chiral angle is calculated with Equation 1.2. The diameter of the SWNT is calculated from Equation 1.3 [20].

$$C_h = n\widehat{a_1} + m\widehat{a_2} \tag{1.1}$$

where C_h is the chiral vector. $\widehat{a_1}$ and $\widehat{a_2}$ are unit cell vectors from the 2D hexagonal graphene sheet. n and m positive integers represent the magnitudes of vectors $\widehat{a_1}$ and $\widehat{a_2}$ which indicates the chirality of the vector.

$$\theta = \cos^{-1}\left(\frac{n+m/2}{\sqrt{n^2+m^2+nm}}\right) \tag{1.2}$$

where θ is the chiral angle. n and m are positive integers that indicate the magnitudes of the vectors $\widehat{a_1}$ and $\widehat{a_2}$.

$$d = \sqrt{3} \cdot \frac{L\sqrt{n^2+m^2+nm}}{\pi} \tag{1.3}$$

where L corresponds to inner atomic layer thickness or the bond length which is taken as 0.142 nm. n and m are positive integers that indicate the magnitudes of the vectors $\widehat{a_1}$ and $\widehat{a_2}$.

The chiral angle is different for different CNT structures. For armchair structure, chiral angle is 30°, for zigzag structure, it is 0°. For the chiral structure, chiral angle takes values between 0° and 30° [20].
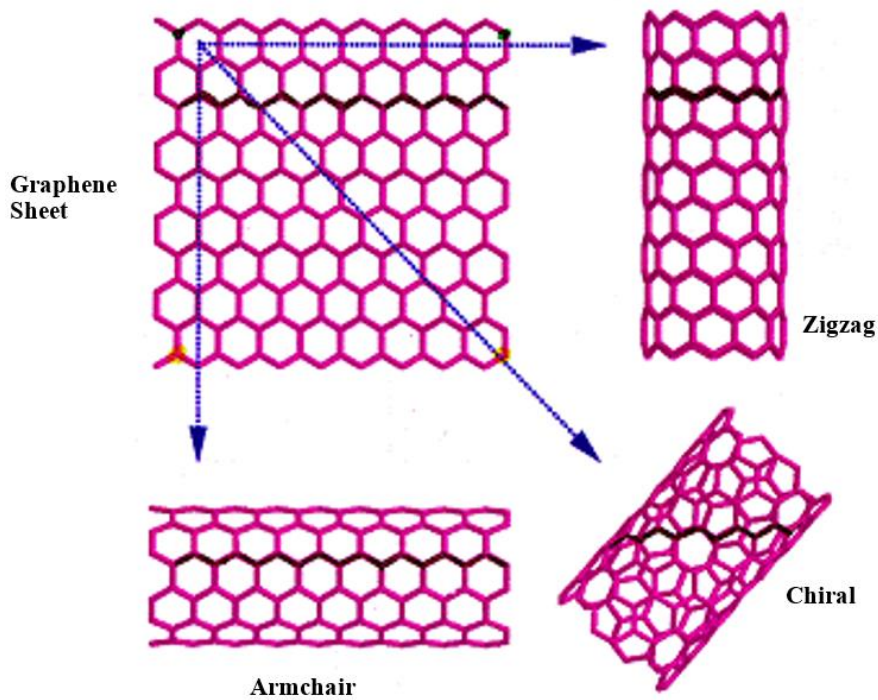
Figure 1.2 Representation of SWNT structures [14]

CNT is categorized according to tube numbers available in a CNT structure. These are single-walled carbon nanotube (SWNT), double-walled carbon nanotube (DWNT), and multi-walled carbon nanotube (MWNT). CNTs have several applications like automotive parts, rechargeable batteries, water filters, and sporting goods. CNTs are produced with the following methods; dry adhesion, terahertz polarization, near-ideal black-body absorption, shape recovery, and high damping [21].

1.5 Composites and Rule of Mixtures (ROM)

The term composite indicates the combination of two or more materials on a macroscopic scale in order to obtain a material with better properties. The main advantage of composites is that they can display the properties of all components. When a composite is formed with different materials, the following properties can be improved; stiffness, weight, strength, thermal conductivity, absorption rates, reflection rates, and so on [22].

The beginning of usage of composite materials is unknown, however, there are examples that composite materials were used by ancient civilizations. For instance, ancient Egyptians (1500 B.C.) used plywood in order to achieve high resistance and strength to thermal expansion. Straw was used to strengthen mud bricks during construction by the Israelites. Also, composites are used in the military as well. Armor and swords were made of different metal composites to have higher strength and toughness (A.D. 1800). Recently, fiber-reinforced matrix composites are popular in use because of having superior properties like high strength and low weight. Modern composites started to be used in the 1930s when resins were reinforced with glass fibers. These glass composites, also called fiberglass, were used to build aircrafts and boats. Composite applications has been widely increasing since 1970s because of the development of new fibers like boron, carbon, and aramids [22], [23].

Mainly a composite is made from two constituents: reinforcement and matrix. The reinforcement mainly provides strength and stiffness. It can be a fiber or a particle. The reinforcement in a composite can be continuous or discontinuous. There is a preferred direction in continuous fibers, whereas discontinuous fibers randomly distributed in a composite. Unidirectional, helical winding, and woven cloth are different examples of continuous reinforcements, while random mat and chopped fibers are examples for discontinuous reinforcements. Fibers are classified according to the aspect ratio they have. Aspect ratio is defined as the ratio of length to diameter. Long aspect ratios are observed in continuous fibers, on the other hand, short aspect ratios are seen in discontinuous fibers. Carbon, glass, and aramid are the most commonly used materials in order to form the fiber [22].

The phase that holds the reinforcement together in a composite is called matrix. This phase generally continuous. The main objective of the matrix is to protect and transmit the load to the reinforcement. The matrix is usually made of polymer, ceramic, or metal [22], [23].

Rule of mixture (ROM) is defined as the equation set that is widely used to calculate mechanical properties of fiber-reinforced composites according to volume fraction of the fiber filler and matrix [24]. It is the volumetric or weight ratio of the fiber to the matrix. Density, elastic modulus, electrical and thermal conductivity are various material properties that can be predicted with ROM [23], [25]. Different variations of ROM are used in this thesis, and they are discussed in methodology and modelling chapter.

1.6 Photovoltaic Effect

Photovoltaic devices convert direct sunlight into direct current (DC) which is then converted to alternating current (AC) to be used as electricity. During electricity generation, several stages occur. These stages are explained with the photovoltaic effect which includes electron and hole pair production and their following collection by the opposite electrodes. The photovoltaic effect is present in both organic and inorganic materials. In organic materials, photon absorption results in delocalization of excited electron-hole pairs while inorganic materials free charge directly produced by photon absorption. Excited electron-hole pairs in organic materials must be separated in order to be transferred by the electrodes [26], [27].

1.7 Bending Deformation Mode

Mechanical loads cause deformation in materials. The deformation can be elastic or plastic which depends on the material and applied stress. This is determined from the elastic curve of the material. In elastic deformation, the object returns to its original shape whereas, in plastic deformation, the final shape of the object is different. Mechanical deformation can be achieved with different loads. In this thesis, bending load and deformation due to bending are investigated. Positive and negative bending of a beam are shown in Figure 1.3.
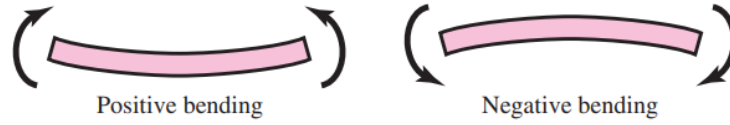
Figure 1.3 Representation of bending according to the direction of the force [28]

When bending load is applied bending stress occur. This bending stress can either be tension or compression. The cross-section of a beam under bending load is shown in Figure 1.4.
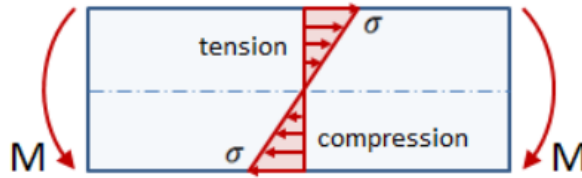
Figure 1.4 Cross-section of a test specimen under bending load [28]

1.8 Absorption, Reflection, and Transmission

Three different phenomena occur when sunlight (electromagnetic radiation) hits the surface of a material. These general phenomena are absorption, reflection, and transmission. There is a well-known relationship between these phenomena. The summation of all there should be equal to 1. This relationship is used to determine the energy percentage of absorbed, transmitted or reflected if the other two are known. This relationship is used in this paper. Because of having an Al ground plate with sufficient thickness, transmitted energy is eliminated. Therefore, absorption only depends on reflection (i.e. absorption + reflection = 1) [29].

1.9 Frequency Spectrum

Frequency spectrum is defined as the distribution of the phases of each frequency component and amplitudes against frequency [30]. Light spectrum distribution with respect to wavelength and frequency is shown in Figure 1.5.

9

The highlighted range corresponds to ultraviolet and visible frequency ranges which are used in this thesis.
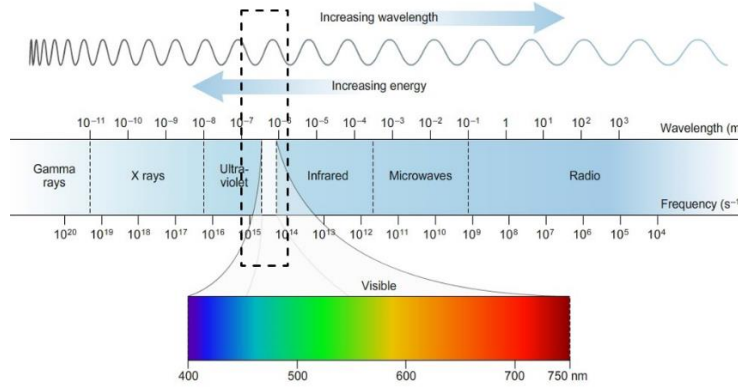
Figure 1.5 Light spectrum chart with respect to wavelength (m) and frequency (Hz) [31]

1.10 Thesis Aim, Objectives, and Overview

The main aim of this research is investigating the effects of bending loads on electro-optical properties of composite based MTM absorbers. To accomplish this aim, several objectives are set for this research. First of all, different and novel MTM absorbers are designed and implemented. Secondly, these designs are simulated without any mechanical load to obtain the electro-optical properties. Thirdly, the change in absorption spectra due to change in polarization angle is investigated. Later on, mechanical bending couple load is applied to the absorbers to examine the change in electro-optical properties. Finally, the surface current distributions, electric and magnetic field distributions are examined.

This research includes literature review in Chapter 2, where the overview of PV technology, review of mechanical impacts on PV modules, theoretical and experimental studies on MTM absorbers, sustainability aspects of MTMs and CNTs, and research gaps are discussed. Chapter 3 explains the details of methodology and modelling that are done in this thesis. Chapter 4 includes validation from literature and S-parameter retrieval. In chapter 5, the design methodology and results of five-strip MTM absorber are presented. Another

absorber design that is generated throughout in this research is presented in Chapter 6, namely, square-strip MTM absorber. Chapter 7 includes the methodology and results behind the last design which is wide-band MTM absorber. In the final chapter (Chapter 8), the conclusions of the thesis and future work are presented.

CHAPTER 2

LITERATURE REVIEW

In this chapter, a detailed literature review is discussed. Firstly, general information about metamaterials and solar cell technology is given. Then, the history of PV technology is discussed. Later, review of mechanical loads that affected solar PV modules is explained with examples. Moreover, previously designed MTM absorbers are reviewed and discussed. Finally, sustainability aspects of metamaterials and carbon nanotubes are discussed.

Metamaterials are materials that have superior mechanical and electrical properties. They can be constructed according to the need [8]. For example, a metamaterial absorber is designed in order to maximize the absorption rate from insolation. This is achieved by integrating CNT into MTM absorber. CNTs are integrated into the substrate part of the MTM absorber.

2.1 Overview of PV Technology

Solar cell technologies have started to have an important role in our life in recent years because of being more economical, sustainable, and environmentally friendly. Since solar cell technology has been advancing fast, the cost of solar cell installed per kilowatt has been decreasing every year in the last decade. According to European Commission PV Status Report in 2017 [32], the newly installed PV capacity is increased to over 79 GW by 38%.

A photovoltaic (PV) module is used to generate electricity directly from the sun. The history of silicon photovoltaic cells reaches to 1954. In 1955, the first PV module was designed for powering telecommunication systems by Bell Laboratories with 2% efficiency. The link between the Bell Laboratories technology and terrestrial applications was achieved by a company called Sharp in Japan in 1959. The company created a small production line for its' Nara Plant in 1964 [33]. With this provided technology, the world's most powerful solar-powered lighthouse with 225 Watt was established on Ogami

Island in 1966 by Sharp company [34]. Increasing absorption rates of solar PV cells and decreasing the $/W rate have been the main objectives of the researchers who work in this area. As shown in Figure 2.1, yearly PV cell production started to increase in early years of 21st century. With the advancement of technology, higher cell efficiencies so that higher power production is achieved [35].
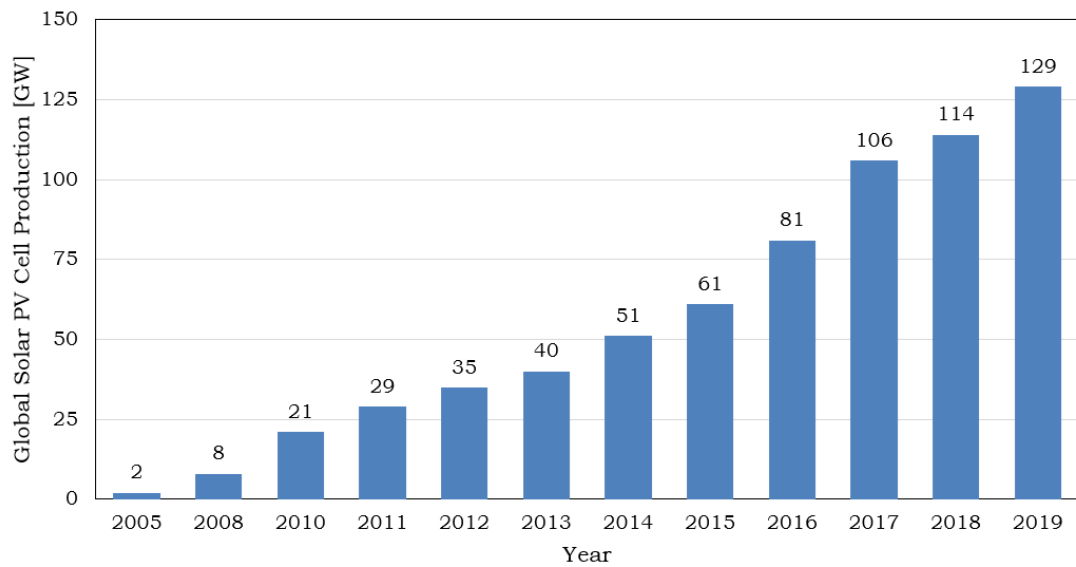
Figure 2.1 Yearly worldwide PV cell production in GW [36]

The most commonly used solar PV devices are shown in Figure 2.2 which summarizes the types and their efficiencies while they are used with large substrates [37]. Photovoltaic technology is divided into crystalline, thin-film, and nanotechnology. The first generation of PV modules involves crystalline structures made of Silicon (Si). The crystalline technology is divided into three sub-technologies; mono-crystalline, poly-crystalline, and EWT (emitter wrap through) [38].

Mono-crystalline cells are the most commonly used PV cells with an 80% market rate. This technology will stay at the lead until another PV technology with higher efficiency and lower cost is found. Crystalline silicon is used with p-n junctions. Mono-crystalline solar cells are manufactured with a method

called the czochral-ski method. The maximum efficiency, at standard test conditions (STC), is around 24% for mono-crystalline solar cells [38].

According to Chaar et al. [38], poly-crystalline solar cells become more popular because of being cost-effective even though their efficiency is around 15%. The main advantage of converting mono-crystalline to poly-crystalline is to reduce the defects on the structure and to decrease metal contamination [39]. The manufacturing process starts with melting and solidifying silicon in order to position crystals in a fixed direction to produce blocks. Then, silicon blocks are sliced into thin wafers [38].
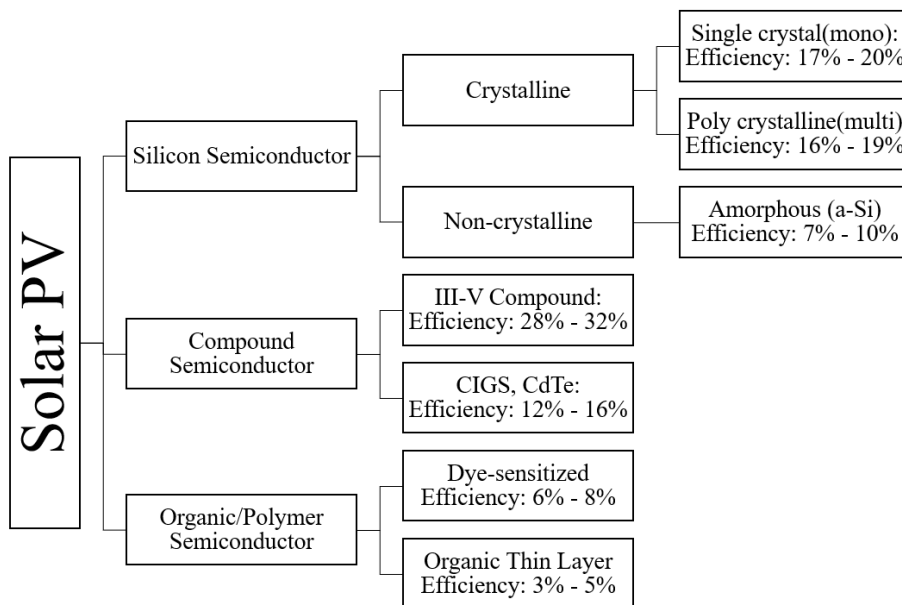
Figure 2.2 Types of Solar PV devices [37]

EWT cells include small holes drilled with laser (see Figure 2.3). These holes are used in order to achieve a connection between the rear n-type contact and opposite side emitter. The advantage of removing front contacts is that it allows the full surface to absorb solar radiation [38].

Thin film technology offers lower costs by reducing material use without endangering the environment and lifetime of the PV cells. Manufacturing thin-film solar cells include depositing thin layers of certain materials on

stainless steel or glass substrates. The main advantage of this method is achieving more flexible solar PV modules. Since layers are much thinner when compared with crystalline types, the cost of producing thin-film PV modules is much less than others. In addition to that, the efficiency of these
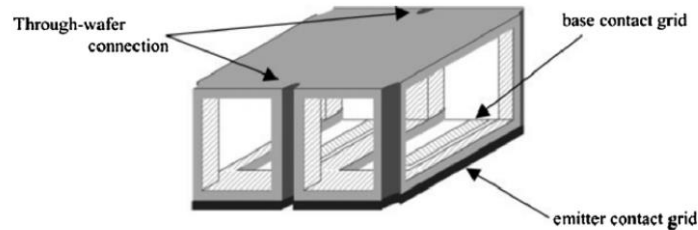
Figure 2.3 Schematic of EWT solar cell [40]

types of PV modules is less than crystalline ones because of having less absorption area. Thin film technology covers around 17% of the PV market according to Chaar et al. [38]. Four types of thin-film cell technology are available in the market; thin polycrystalline silicon cell, the amorphous silicon cell, the cadmium telluride/cadmium sulfide hetero-junction cell, and the copper indium diselenide/cadmium sulfide hetero-junction cell [38].

2.2 Review of Mechanical Impacts on PV Modules

PV modules face mechanical impacts and mechanical loads during manufacturing, during transportation, and during operation. Vibrations and loads during operation and during transportation can cause stress on PV cells which results in cracks. Due to these loads, cell failure can be observed. Moreover, thin-film PV modules can encounter cell corrosion problem because of the bias voltage that occurs during operation [6], [7].

As mentioned before, mechanical loads cause randomly distributed cracks on PV modules. They may occur during different periods of module lifecycle. For example, in the soldering stage of the PV module manufacturing process, high stresses are applied to PV modules which are considered as the reasons for cracks. Additional to the cracks occurred during manufacturing and

transportation, they may occur during operation due to environmental impacts like wind and snow [41], [42].

There are different tests that a solar PV module face during manufacturing. IEC standards examine the static and dynamic uniform wind loads on PV modules. Static mechanical load, dynamic mechanical load tests are applied according to ICE standards for uniform load distribution. Static snow load is also applied according to ICE standards to PV modules with a non-uniform load. Moreover, Hsu et al. [43], developed two analytical models in order to simulate the uneven wind loads on PV modules during operation. These models are mean extended wind load test method (MEWL) and non-uniform dynamic mechanical load system (NUDML). According to these tests, MEWL test depends on the environmental conditions like inclined angle of the PV module, wind direction angle, and wind velocity. Gul et al. [44] designed and constructed a test setup according to the international standards in order to observe the reaction of the PV module under wind load. Four 60W commercially available PV modules were used in this study. After the mechanical loads were applied, the electrical efficiency test and electroluminescence are applied. According to results of these tests, peak power output of the PV modules is decreased by 2%. Average 0.20% decrease in fill factor is also observed [44].

There are different experiments in the literature about mechanical loads on PV modules. Mickiewicz et al [45] designed a mechanical test stand which can fit up to 550 mm x 550 mm PV modules, so that, mechanical impacts on PV modules at different temperatures were investigated. The mechanical stand was put on a climate chamber, then a uniform load with a range between 2.4 kPa and 10 kPa pressure was applied with compressed air. A number of PV modules were used in the test that consisted of a PET back sheet, two 3-cell strings with 156 mm multi-crystalline solar cells, and a glass plate on the front with 550 mm x 405 mm dimensions and 3.2 mm thickness. Moreover, two different encapsulates, an industry-standard EVA and a Dow Coining silicon, were used in the tests. According to the results of the

experiments, the modulus of EVA increased significantly between -30 °C and ambient temperature which indicates the encapsulation material becomes stiffer in lower temperatures. On the other hand, the encapsulation with silicon had more stable and lower modulus within the temperature range of the test [45].

Zhang et al. [46] investigated the bending behavior of PV modules under uniformly distributed load by both theoretical and experimental work. The theoretical part of the research included that the classical laminate theory model (Hoff Model) and modified Rayleigh-Rita method were used in this research in order to develop a closed-form solution. Boundary conditions for theoretical work were adopted as two opposite edges simply supported and other two remained free, i.e. no force or support was applied. For the experimental part of the work, water pressure was applied in order to obtain the uniformly distributed load on PV module. A special structure was manufactured so that the previously mentioned boundary conditions were simulated. 8 specimens were used in the bending experiments at room temperature. As mentioned before, Hoff model used to simulate the bending operation. Finite element analysis was done with ANSYS software in order to obtain stress and deflection analysis of PV modules. According to both theoretical and experimental results, the maximum stress and deformation were located in the middle of the PV module. Simulations by ANSYS, experimental work and calculations via proposed equations gave similar results in this research [46].

Suzuki et al. [47] designed and manufactured a test setup in order to investigate the effects of tensile and compressive stresses at different temperatures on PV modules. The test setup included a climate chamber, bending setup, and PV modules. Three multi-crystalline p-type PV cells were used in the experiment. Copper is used to connect the PV cells, and lamination was achieved by using a three-layered back-sheet made of polyvinyl fluoride (PVF), polyethylene terephthalate, and PVF. The electrical characteristics of PV modules were taken as in the standard test conditions

(25°C, 1000 W/m², 1.5G air mass). Bending cyclic load test applied to the horizontally placed PV module. A 500 Newton cyclic unidirectional bending load was applied to the module for 10 000, 20 000, or 30 000 loading cycles at -20°C, +25°C, and +80°C temperatures. According to the experimental results, regardless of bending direction, large number of cracks occurred in lower temperatures (-20°C). Low number of cracks occurred in moderate temperatures (+25°C). At high temperatures (+80°C), no cracks were present [47].

Table 2.1 shows the summary of the literature that investigates the impacts of different mechanical loads on PV modules.

Table 2.1 Summary of review of mechanical impacts on PV modules from the literature [43], [44], [46], [47]

Reference	Test	Details	Results
Hsu Et al.	2 Analytical Models	MEWL: Mean Extended Wind Load Test Method NUDML: Non-uniform Mechanical Load System	MEWL depends on environmental conditions; inclined angle of PV module, wind direction & velocity
Gul et al.	Test setup according to International standards	Aim: Observing the reaction of PV module under wind load	Peak power output of PV: decreased 2%
Zhang et al.	Bending behavior of PV modules	Uniformly distributed load is applied to a classical laminate theory model. Water pressure is used to apply uniform load	Maximum stress and deformation occurred in the middle of the PV module
Suzuki et al.	Tensile and compressive stress	Investigating the effects of tensile and compressive loads at different temperatures Bending load: 500 N cyclic load	Regardless of bending direction, Lower Temp: high number of cracks Moderate Temp: Low number of cracks High Temp: No cracks were present

2.3 Theoretical and Experimental Studies on MTM Absorbers

In this part of the thesis, the review of metamaterial absorbers is presented in detail. Since the first so-called perfect metamaterial absorber is presented in 2008 [48], work on different types of metamaterial absorbers has been increased in the last decade. These types include dual-band, single-band, multi-band metamaterial absorbers. Metamaterial absorbers are categorized according to their shape, material, resonator type, and absorption response. As a result of doing a literature review on metamaterial absorbers, five different designs are investigated and presented in this part of the thesis, and they are shown in Table 2.2.

The first metamaterial absorber in the literature is designed and presented by Landy et al. with the title of "perfect metamaterial absorber" [48]. This design includes a single unit cell with a split ring resonator in the front and a metallic split-wire at the back. The electrical coupling on this absorber is achieved with an electric ring resonator. The representation of this metamaterial absorber can be seen in Figure 2.4 (a). The split ring resonator in the front is made of two standard split-ring resonators, and the connection between them is achieved with the inductive ring parallel to the split wire.
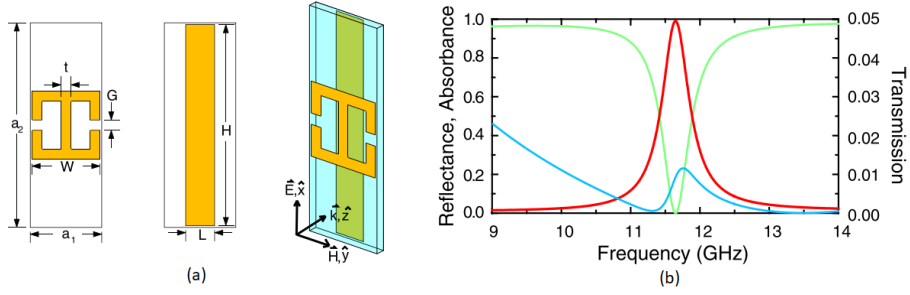
Figure 2.4 Unit cell design of "Perfect Metamaterial Absorber" (a), and frequency response of the design (b), red color represents absorption, light green color represents reflection, transmission represented with light blue color [48]

The front and back resonators are separated with the FR4 substrate. Finite difference time domain solver of software called CST Microwave Studio is used in order to do the simulations. The boundary conditions include perfect magnetic on xz-plane and perfect electric in yz-plane. The results of the simulations are presented with a maximum absorption rate of 96% at 11.65 GHz and the results are shown in Figure 2.4 (b) [48].

Unlike standard microwave absorbers that have large thickness, Ghosh et al [49] designed an ultrathin metamaterial absorber. The design consists of an FR4 dielectric substrate in the middle, a periodic swastika-like structure made of copper at the top, and a copper ground plate at the bottom. The structure is presented in Figure 2.5 (a). There is no transmission observed because of the copper ground plate. Therefore, the absorption response of the absorber only depends on the reflection rate. Frequency structure simulator

19

is used with periodic boundary conditions. As a result of the simulations, 99.64% absorption rate is achieved at 10.10 GHz frequency as can be seen from Figure 2.5 (b).
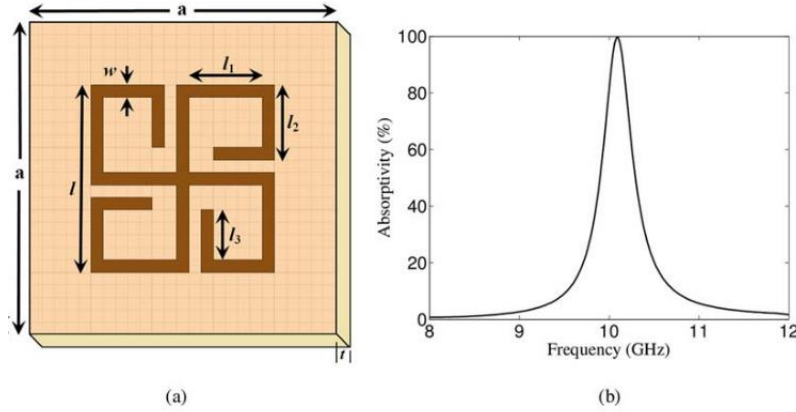
Figure 2.5 Structural representation (a), simulation results (b) of ultrathin polarization-insensitive microwave absorber design [49]

The bandwidth-enhanced structure is achieved with 2 x 2 array of the structure. It is presented in Figure 2.6 (a). The four structures are identical. Periodic boundary conditions are applied during the simulation, so that, two absorption peaks occurred with 93.63% and 91.39% at 10.24 GHz and 10.50 GHz. The results are shown in Figure 2.6 (b). The results of both simulations are validated via experimentation [49].
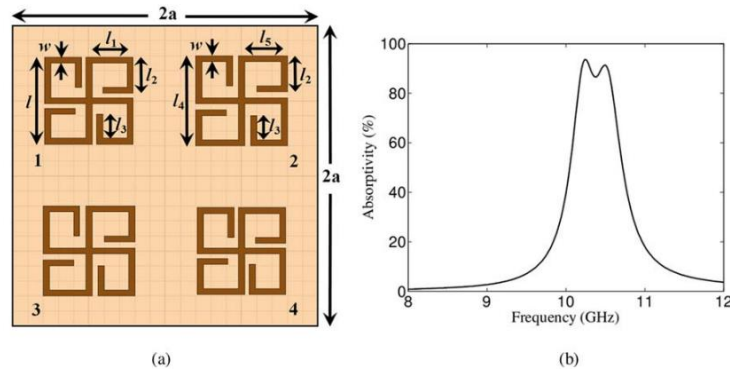
Figure 2.6 2 x 2 bandwidth-enhanced structure (a), simulation results (b) for ultrathin polarization-insensitive microwave metamaterial absorber [49]

The unit cell metamaterial absorber designed by Ma et al. [50] includes a cross resonator and four split-ring resonators made of gold (Au). The middle layer is made of SiO_2 that is sandwiched by the front resonators and a gold ground plate. The schematic of the unit cell is shown in Figure 2.7 (a). Finite difference time-domain simulation is carried away with a commercial software called CST Microwave Studio. Time-domain solver of the software is used with the required boundary conditions in order to get the absorption and reflection rates of the MTM absorber. The transmission rates are also neglected because of having a golden ground plate with sufficient thickness. Moreover, experimental and calculated results are also presented in this design. A microscope coupled Fourier transform infrared spectrometer is used to record the power reflection of the dual-band MTM absorber. According to the measurement, simulations, and calculations, the MTM absorber has two absorption peaks with 90.3% and 88.4% at 4.17 µm and 4.86 µm wavelengths, respectively. These results are plotted together and presented in Figure 2.7 (b) [50].
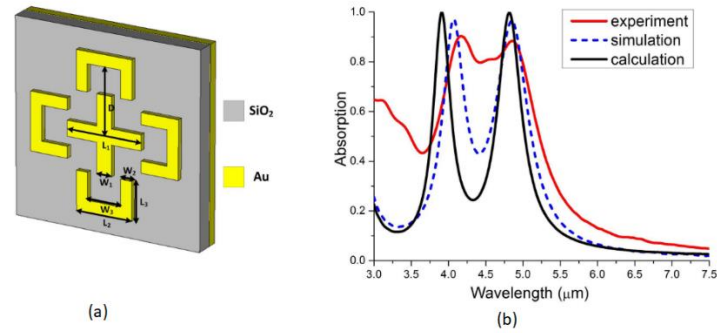
Figure 2.7 Schematic diagram of the unit cell (a), simulation, experimental and calculation results of the metamaterial absorber designed by Ma et al. [50]

Wang et al [51] proposed a polarization-insensitive and four-band terahertz metamaterial absorber in 2015. The MTM absorber consists of a metallic ground plate made of gold, a dielectric layer, and four-square golden rings. The proposed metamaterial absorber is presented in Figure 2.8. The electric field distribution on the absorber is investigated in order to understand the

theory behind this four-band absorption mechanism. Also, the absorption performance is analyzed by an equivalent LC resonant circuit model [51].
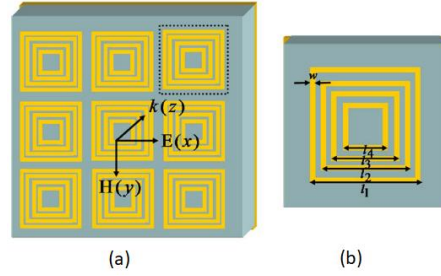
Figure 2.8 Proposed MTM absorber design of Wang et al (a), and unit cell representation of the MTM absorber (b) [51]

According to the simulation results shown in Figure 2.9, four different absorption rates with a 97% average at 0.777, 1.13, 1.53, and 2.06 THz frequencies are obtained. Four-band absorption mechanism is achieved because four different resonant frequencies overlapped. According to Wang et al [51], the absorption peaks can be increased by increasing the number of front resonators (i.e. square metallic rings). This particular MTM absorber has a potential to be used in imaging, detection, and stealth technology.
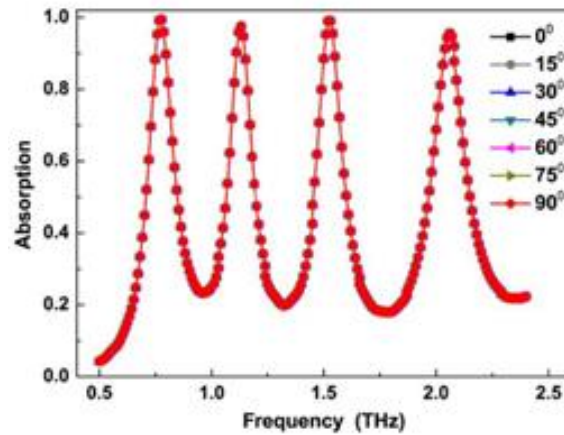
Figure 2.9 The simulation results with respect to polarization angles of the incident wave for the proposed MTM absorber by Wang et al. [51]

Ghosh et al [52] proposed an ultra-wideband ultrathin metamaterial absorber which operates in the microwave frequency regime in 2015. This design

22

includes two concentric circular split rings, a dielectric substrate and a metal ground plate which can be seen in Figure 2.10 (a). FR-4 dielectric substrate with 2 mm thickness is used in the middle. At the top, two concentric split rings made of copper with a thickness of 0.035 mm. The ANSYS HFSS software is used to the simulations with periodic boundary conditions. This paper also uses the same phenomenon as previous ones. This phenomenon is explained as summation of absorption, reflection, and transmission is equal to 1. Since the proposed structure has a ground plate, transmission is taken as zero. Therefore, absorption only depends on the reflection rate of the absorber. The results of the simulations are presented in Figure 2.10 (b) which shows that absorption rate above 90% between 7.85 and 12.25 GHz frequencies. Moreover, two absorption peaks are seen as 99.66% and 99.92% at 8.36 GHz and 11.18 GHz, respectively. The results presented in Figure 2.10 (b) show similarities with the experiments done within this study. According to the authors, this absorber is suitable to be used in electromagnetic compatibility, electromagnetic interference, and stealth technology [52].
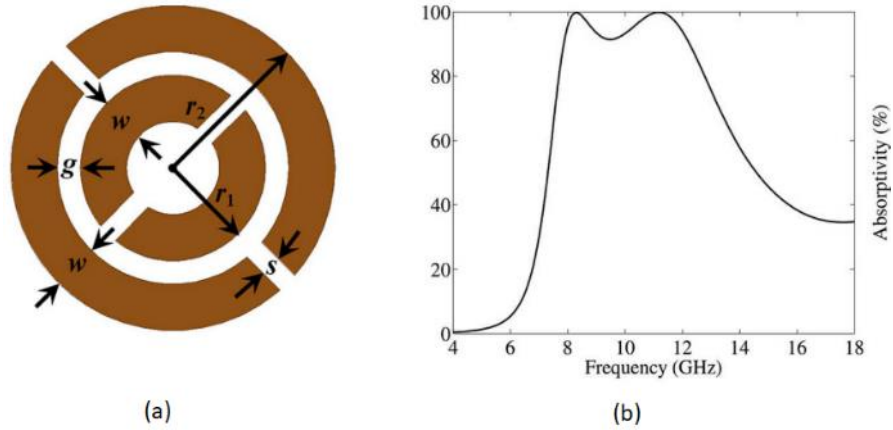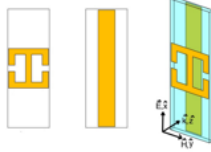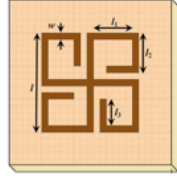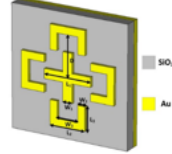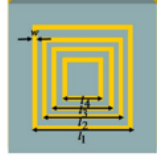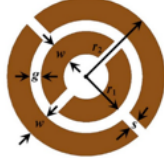
Figure 2.10 Proposed MTM absorber (a), and simulation results (b) by Ghosh et al [52]

The summary of the literature review of the previously designed metamaterial absorbers is presented in Table 2.2.

Table 2.2 Summary of previously designed metamaterial absorbers from the literature [48]–[52]

Reference	Year	Details	Results	Structure
Landy et al.	2008	Front: split ring resonator Back: metallic split-wire 2 split ring resonators Connected via inductive ring parallel to split-wire	Maximum absorption: 96% at 11.65 GHz	
Ghosh et al.	2014	FR4 Substrate A periodic array of swastika-like FR4 dielectic substrate Copper ground Plate Symmetric structure	99.64% absorption at 10.10 GHz 81% absorption up to 60° incident angle	
Ma et al.	2014	Infrared dual-band MTM absorber SiO_2 & Au	Peak of 90.3% at 4.17 µm Peak of 88.4% at 4.86 µm	
Wang et al.	2015	A dielectric layer 4 square metal rings A metallic ground plate	4 absorption peaks 97% average With 0.777, 1.13, 1.53, 2.06 THz	
Ghosh et al.	2015	2 concentric circular split rings Metal-backed substrate Different polarization angles	10-dB absorption Bandwidth From 7.85 to 12.25 GHz	

2.4 Sustainability Aspects of Metamaterials

Sunlight is one of the cleanest and sustainable energy resources of the Earth [2]. There are a lot of studies regarding conversion of sunlight into pure energy. One of these ways is using Solar PV modules which directly converts sunlight into electricity [3], [4]. However, the efficiency of the currently available PV modules is around 22% which means that currently available PV modules converts only 22% of the sunlight that hits the module [2]. Metamaterial absorbers are proposed and furtherly investigated in order to increase this conversion rate [5]. Metamaterials are used in different fields as

24

mentioned before. In this section of the thesis, sustainability aspects of metamaterials will be investigated and explained.

As mentioned before, metamaterials are used as absorbers. These MTM absorbers can be used in energy field and sensor field. An MTM absorber have a tendency to increase the efficiency of a solar cells when it is integrated on the cell [53].

Biosensors made of metamaterials can be used in environmental monitoring in order to detect different pollutants like heavy metals, surfactants, pesticides, and so on [54]. By using metamaterial based biosensors, some materials that may be harmful to the environment can be detected because a metamaterial biosensor can operate in low and high frequency ranges [55].

In this thesis, the MTM absorber consists of a substrate made of silicon-carbon nanotube composite and Aluminum metal layers. The composite contains 5% CNT, the rest is made of silicon. The details of the composite are explained in Methodology and Modelling chapter. Since CNT has superior properties when compared to Silicon which is the main substance that is used when manufacturing a solar cell, integrating CNT into substrate of the absorber will result in higher efficiencies for the solar cells [56]. As stated before, all metal layers of the absorber are made of aluminum metal because it has lower skin depth, maximum reflection, high temperature resistance, and it is cheaper when compared to other metals. Thus, the objective will be achieved with less material and lower cost [56], [57].

During operation, an MTM absorber does not emit greenhouse gasses, it is environmentally friendly and does not pollute the environment. Moreover, the contribution to the solar energy field via increasing the efficiency of a solar cell, increases clean energy generation for sustainable development [58].

Because of the reasons mentioned in this section, designing an MTM absorber with Si-CNT composite and aluminum can be a sustainable solution

in order to increase the solar cell efficiency, and hence increasing clean energy generation.

2.5 Sustainability Aspect of Carbon Nanotubes

Carbon nanotubes (CNTs) are the most researched and investigated nanoparticle among researchers because of having outstanding magnetic, optical and electronic properties [59], [60]. They have a huge role in the advancement of the sustainable development. Additionally, they are used to generate sustainable solutions to the energy problem that we have been facing because of continuous increase in the energy demand [61].

Carbon nanotubes display key features in developing advanced sustainable materials for energy applications: high chemical stability, high mechanical strength, excellent electrical properties, high activated surface area, and high aspect ratio [62]. CNTs can be used as pure or as a composite with other metals which plays a key role in advancements of carbon-based electronic devices like supercapacitors, fuel cells, photovoltaic devices, and Li-ion batteries [61].

Supercapacitor is defined as an energy conversion device that uses the physical principles of energy storage and merges advantages of batteries based on capacitors and electrochemical redox processes [63]. The role of CNTs in supercapacitor applications is enhancing the transfer of ions from the electrolyte to the entire surface of the electrodes which is achieved by having a well-developed network form. This results in quick response to an external potential charge. Thus, the capability of energy extraction is increased at high frequencies [61]. Supercapacitor is used in hybrid and solar cars [64].

A lithium ion battery is a rechargeable battery that is commonly used in hybrid cars and solar cars. The discharge and charging is possible with back and forward movement of lithium ions between positive electrode and negative electrode [65]. CNTs are integrated to the lithium ion batteries

because they increase the conductivity and absorptivity. In addition, high temperature operations are also possible while CNTs are used [66]. However, there is a drawback to the CNT applications because they are not cost effective. In other words, CNT based batteries are not economically feasible to use in commercial products [61].

CNTs are used in manufacturing of dye-sensitized solar cells (DSSCs) because of being flexible, having low electrical resistance, and having excellent mechanical integrity. DSSCs are an alternative choice for the current p-n junction PV cells. They are categorized as photoelectrochemical solar devices that incorporate dye molecules into semiconductor oxides within the system [67]. CNTs are the best choice for a solar cell when compared to other metallic substrate materials like gold, silver, etc. because they have interactive surface area, high electrochemical activity, and high aspect ratios [68].

CNTs are also used in water treatment technologies because of having tunable and unique structure, excellent chemical, mechanical, electrical, and physical properties. They can be solution to various environmental problems. They can be used as absorbents in order to remove some organic and inorganic pollutants from the water resources. They are also used as catalysts and co-catalysts for bio-refractory and persistent organic pollutants [69].

2.6 Research Gaps

There are several studies in the literature that have been carried out about designing a perfect MTM absorber for solar cell applications [48]–[52]. These studies include both experimental and theoretical works. The main point that these studies focus on is having a perfect MTM absorber. To do so, the geometry and dimensions were changed in the mentioned studies. It can be stated that there are few studies that focus on the mechanical impact on these designed MTM absorbers. Investigating the impacts of mechanical loads and forces on MTM absorbers creates a great opportunity for research. Moreover, the MTM absorber studies in the literature usually have a

substrate made of a single material, i.e. not a composite (e.g., [48]–[52]). This creates a great opportunity to use a composite as a substrate on the MTM absorber. Furthermore, there were not enough studies on the sustainability aspects of MTM absorbers. Overall, this study aims to contribute to the literature in order to shed light onto the aforementioned gaps. In brief, the research gaps are listed as below:

- Change in absorption rates due to mechanical loads.
- Using composite substrate.
- Frequency tunning with deformation.
- Dual-band response with deformation.

The main objectives of this research are listed as follows.

- Designing MTM absorbers with different geometries.
- Carrying out simulations with and without bending load by using Finite Integration Technique.
- Investigating the change in absorption spectra due to different polarization angles.
- Determining the change in the electro-optical properties under bending loads.

CHAPTER 3

METHODOLOGY AND MODELLING

In this part of the thesis, the methodology behind the simulations and calculations are discussed. Relevant theory and related equations are presented. Three metamaterial absorbers are designed with different front resonator geometries.

The proposed MTM absorbers are made of Aluminum (Al) and Silicon-Carbon Nanotube (Si-CNT) composite. Aluminum metal is used in the ground plate and front resonators for all MTM absorbers designed in this thesis. The reason behind using aluminum metal is that it is cheap, a good reflector, and environmentally friendly [14].

3.1 Analysis Approach

Finite integration technique (FIT) is used to analyze the electrical properties (i.e., absorption, reflection) of the proposed MTM absorber. Frequency-domain solver is applied in order to examine the absorption behavior of the proposed MTM structure. This technique requires boundary conditions for x, y, and z-directions. In this thesis, electric (E), magnetic (H), and open add space boundary conditions applied. E-field in the x-direction, H-field in the y-direction, and open add space condition are applied in the z-direction. This technique requires surface meshing [70]. Three different phenomena occur when sunlight (electromagnetic radiation) hits the surface of a material. These are absorption, reflection, and transmission. There is a well-known relationship regarding these phenomena which is shown in Equation 3.1 [15], [71].

$$A(w) + R(w) + T(w) = 1 \qquad\qquad (3.1)$$

$$R(w) = S_{11}^2 \qquad\qquad (3.2)$$

$$T(w) = S_{21}^2 \qquad\qquad (3.3)$$

where $A(w)$, $R(w)$, and $T(w)$ represent absorbance, reflectance, and transmittance, respectively. Reflectance is calculated using Equation 3.2, whereas transmittance is calculated via Equation 3.3. S_{11} represents reflection, and S_{21} represents transmission.

This relationship is used to determine the energy percentage of either absorbed (A), transmitted (T), or reflected (R) sunlight if the other two are known. The current work adopts this formulation as a basis for the calculations. Due to having an Al ground plate with sufficient thickness, transmitted energy is regarded as eliminated. Therefore, absorption only depends on reflection (i.e. Absorption + Reflection = 1) [29].

In order to analyze the mechanical deformations and mechanical stresses, finite element modeling (FEM) is used. This modeling simulation requires 3D meshing which is dividing the structure into small elements. There are different types of meshing for different applications. In this thesis, tetrahedral mesh is used in order to examine the mechanical stresses.

In finite element method and finite integration technique, the structure is divided into small elements called mesh. Each of these small elements is called a mesh cell. Selecting the size and the type of the mesh has a crucial role in performing finite element analysis and electromagnetic simulations. The type, the size, and the density of the mesh determine the speed and accuracy of the simulations. In this research, tetrahedral mesh type is used with "adaptive mesh refinement" which increases the number of meshed cells according to the specified accuracy level that is $1\text{x}10^{-6}$ in this research. Adaptive mesh ensures sufficient mesh density in order to have reliable, accurate, and valid results.

In this thesis, the mechanical load that is applied on the absorbers is selected to be the bending deformation. The main reason behind this selection is that the use of bent solar PV modules have been increasing [72], [73]. This bent modules are used in several applications: solar cars [74], bus stops, top of parking lots [75] etc.

3.2 Silicon – CNT Composite

To obtain the properties of Silicon-CNT composite, different combinations of the rule of mixtures are used. In rule of mixtures, there are two components, fiber, and matrix. In this thesis, fiber is CNT with 5%, and matrix is Silicon with 95%. The reason behind this rate is that, after conducting a wide literature review, one of the maximum and widely preferred rates of CNT used in a composite is suggested to be 5% [76]. Thus, 5% CNT is selected while obtaining the composite structure.

Young's Modulus is defined as the ratio of stress over strain. Hooke's law is used to determine the young's modulus of a material if the material is in elastic range. Hooke's law is shown in Equation 3.4 [77], [78]. Young's modulus of a composite material is found from Equation 3.5 [23].

$$\sigma_s = E \cdot \epsilon \tag{3.4}$$

where σ_s is stress on the material, ϵ is the strain and E is the young's modulus.

$$E_c = E_f \cdot V_f + E_m \cdot V_m \tag{3.5}$$

where E_c is the young's modulus for the composite, E_f and E_m are young's modulus for fiber which is CNT and matrix which is Silicon, respectively. V_f and V_m are volume fractions for fiber and matrix respectively.

The density of the composite can also be calculated with rule of mixtures which is shown in Equation 3.6 [23].

$$\rho_c = \rho_f \cdot V_f + \rho_m \cdot V_m \tag{3.6}$$

where ρ_c is the density of the composite. ρ_f and ρ_m are densities of fiber and matrix respectively. V_f and V_m are volume fractions of fiber and matrix.

Poisson's ratio is the measure of the deformation in the material's transverse direction to longitudinal direction. It is an elastic constant [77]. Poisson's ratio for the composite is obtained from Equation 3.7 [23].

$$v_c = v_f \cdot V_f + v_m \cdot V_m \tag{3.7}$$

where v_c is the Poisson's ratio of the composite. v_f is the Poisson's ratio of the fiber, v_m is the Poisson's ratio for the matrix. V_f and V_m are volume fractions for fiber and matrix.

Thermal conductivity is defined as the capability to conduct heat. Heat transfer rate is high in materials that have higher thermal conductivity. It is influenced with chemical compositions in the material, temperature, and the microstructure of the material [79], [80]. The thermal conductivity of composite material is obtained from Equation 3.8 [81].

$$k_c = \left[\frac{(1 - V_d)}{k_m} + \frac{V_d}{k_f} \right]^{-1} \tag{3.8}$$

where k_c is the thermal conductivity of composite material. V_d is the volume fraction of fiber to matrix. k_f is the thermal conductivity of fiber material, and k_m is the thermal conductivity of matrix material.

Electrical conductivity is the measure of the amount of electric current passing through an object. Its unit is reciprocal ohm meters ($\Omega^{-1}m^{-1}$) [82]. The electrical conductivity of a composite is calculated from Equation 3.9 [83].

$$\sigma_c = \sigma_f \cdot V_f + \sigma_m \cdot V_m \tag{3.9}$$

where σ_c is the electrical conductivity of the composite material. σ_f is the electrical conductivity of the fiber material and σ_m is the electrical conductivity of matrix material. V_f and V_m are volume fractions of fiber and matrix materials, respectively.

Heat capacity is a physical measure that distinguishes the required heat amount in order to change an objects' temperature with a given amount. It is used to determine the required heat amount and processing temperatures for a material [84], [85]. Heat capacity of the composite is calculated from Equation 3.10 [86].

$$K_c = K_m \cdot \frac{1 - V_d}{1 + 0.5 \cdot V_d} \tag{3.10}$$

where K_c is the composite heat capacity. K_m is the heat capacity of the matrix, and V_d is the volume fraction of fiber to the matrix (i.e. $V_d = V_f/V_m$)

The thermal expansion coefficient is described as the amount of volumetric change of a material because of temperature change. Thermal expansion coefficient of a composite mainly depends on environment, components of the composite, and state of the composite [87], [88]. The thermal expansion coefficient of the Si-CNT composite can be calculated with Equation 3.11 [89].

$$\alpha_c = \frac{V_f \cdot \alpha_f \cdot E_f + V_m \cdot \alpha_m \cdot E_m}{V_f \cdot E_f + V_m \cdot E_m} \tag{3.11}$$

where α_c is the thermal expansion coefficient of the composite material. α_f is the thermal expansion coefficient for fiber material, and α_m is the thermal expansion coefficient of matrix material. E_f and E_m are Young's modulus of fiber and matrix materials, respectively. V_f and V_m are volume fractions for fiber and matrix materials.

The yield strength of the composite is calculated according to the iso-strain model which is shown in Equation 3.12. Iso-strain models assume same stress occurs on both matrix and fiber during deformation [90].

$$Y_y = Y_f \cdot V_f + Y_m \cdot V_m \tag{3.12}$$

where Y_y is the yield strength of the composite material. Y_f is the yield strength of the fiber material and Y_m is the yield strength of matrix material. V_f and V_m are volume fractions of fiber and matrix materials, respectively

Table 3.1 shows the material properties of the Si-CNT composite. The composite properties are calculated according to previously mentioned equations. As seen in Table 3.1, the Si-CNT composite contains 5% CNT. With the rule of mixtures and other equations, material properties for Si-CNT composite are calculated via MS Excel. Material properties mentioned in Figure 3.1 are entered into the software in order to create the required composite.

Table 3.1 Mechanical and electrical properties of CNT, Silicon, and the composite which are obtained according to Rule of Mixtures

Property	Material		
	CNT	Silicon	Composite
Electrical Conductivity (S/m)	1.00E+05 [91]	2.50E-04 [92]	5000.00
Density (g/cm^3)	1.16 [93]	2.33 [94]	2.27
Young's Modulus (GPa)	881.00 [95]	107.00 [92]	145.70
Thermal Conductivity (W/mK)	3500.00 [96]	130.00 [97]	136.94
Poisson's Ratio	0.28 [95]	0.28 [92]	0.28
Heat Capacity (J/kgK)	494.30 [98]	710.00 [97]	655.38
Thermal Expansion Coefficient (1/K)	2.00E-05 [99]	2.60E-06 [92]	7.86E-06
Yield Strength (GPa)	90 [100]	3.97 [101]	8.27
Volume (%)	5.00%	95.00%	100.00%

CHAPTER 4

VALIDATION

One of the most crucial parts of this research is validation because it is important that the simulated results are accurate and reliable. Hence, this chapter includes the verification of the obtained results that is achieved with validation from the literature and S-parameter retrieval.

4.1 Validation from Literature

Numerical validation is achieved by comparison between the simulation results and an experimentally verified work from the literature. The experimental work was conducted by Shen et al. [102] who proposed and experimentally verified a triple-band terahertz metamaterial absorber that operates between 0 and 2.5 THz. The major results of the study were having three absorption peaks at 0.5, 1.03, and 1.71 THz. The proposed absorber was made of three layers, resonator, a dielectric layer, and a back-metal plane. The resonator was made of three concentric Aluminum square rings with different dimensions as W_1 = 84 μm, W_2 = 56 μm, W_3 = 36 μm, line width W = 5 μm, and thickness of 0.2 μm. The back-metal plane was also made of Aluminum with thickness of 0.2 μm. The resonator was made of Polyimide which was taken as lossy metal with ε = 2.9 dielectric constant and tan(δ) = 0.02. The isometric view of the three-band terahertz absorber designed by Shen et al. is shown in Figure 4.1.

The same structure shown in Figure 4.1 is modelled in the simulation software that is used to simulate the results obtained in this thesis. In the simulations, the boundary conditions are taken as electric field at x-direction, magnetic field in y-direction, and open add space at z-direction. Tetrahedral mesh type is selected with adaptive mesh refreshments. Equation 3.1 from the analysis approach section is used to determine the absorption curve. Figure 4.2 shows the numerical simulation results and the experimental results obtained by Shen et al. [102]. In Figure 4.2, our simulation is

presented with yellow dashed-line (Sim*) which matches with the Shen et al. simulation (Sim), experiment (Exp) and calibrated (Cal) results. With the verification of experimental data, it can be concluded that the simulation results carried out in this thesis are validated.
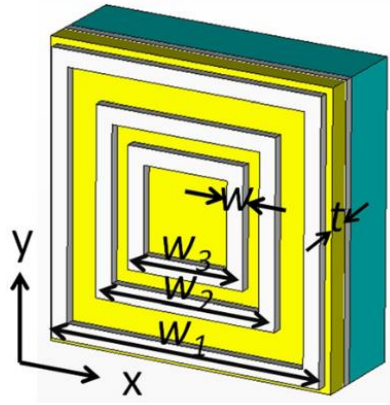
Figure 4.1 Isometric view of the triple-band terahertz metamaterial absorber designed by Shen et al. [102]
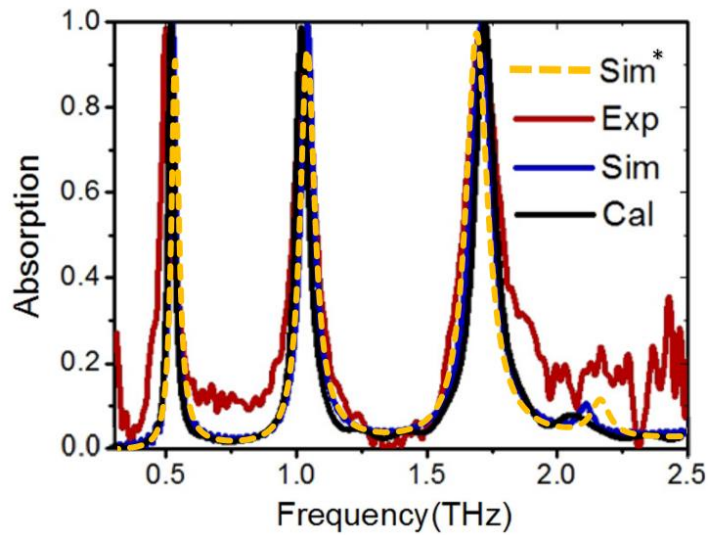
Figure 4.2 Numerical comparison of the simulated results and experimental results by Shen et al.

4.2 S-parameter Retrieval

The most critical parameters to define the electromagnetic characteristics of a material structure are permittivity and permeability. They are used to obtain the response of a material to the incoming electromagnetic radiation (sunlight). In order to determine whether the proposed absorber is a left-handed material or not, these parameters should be extracted with respect to each frequency. In this part of the thesis, the wide-band Si-CNT based metamaterial absorber (See Figure 7.1) is inspected for S-parameter retrieval. To do so, the refractive index and impedance of the material will be used to extract the permittivity and permeability. First of all, refractive index and impedance are obtained through S-parameters. S-parameters are obtained with the appropriate boundary conditions through THz waves sent from ports. The demonstration of reflected and transmitted electromagnetic waves is shown in Figure 4.3. The real metamaterial slab is represented in Figure 4.3 (a), however, since the combination of two materials will negatively affect the total refractive index and impedance in terms of having different geometries and thicknesses, it is nearly impossible to simplify the refractive index. Thus, the metamaterial absorber is assumed to be a homogeneous slab as seen in Figure 4.3 (b). With this assumption, the required parameters are calculated by using the S-parameters that are generated throughout the simulations.
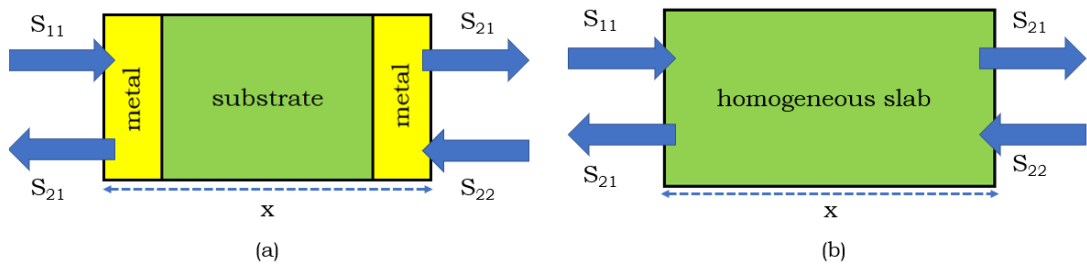
Figure 4.3 Demonstration of scattering parameters through real design (a) and homogeneous assumption (b)

Reflection coefficient is calculated via Equation 4.1 [103].

$$r = \frac{z-z_0}{z+z_0} \tag{4.1}$$

where r is reflection coefficient and z is the impedance.

The transmission coefficient is obtained from Equation 4.2 [103].

$$t = e^{j \cdot k_0 \cdot p \cdot d} \tag{4.2}$$

where t is the transmission coefficient, d is the maximum length of the structure, k_0 is the wave number, and p is the refractive index.

After the determination of reflection and transmission coefficients, by using Equation 4.1 and 4.2, S_{11} and S_{21} can be retrieved from Equations 4.3 and 4.4 [103].

$$S_{11} = \frac{r \cdot (1-t^2)}{1-r^2 \cdot t^2} \tag{4.3}$$

$$S_{21} = \frac{t \cdot (1-r^2)}{1-r^2 \cdot t^2} \tag{4.4}$$

The impedance can be calculated by using Equation 4.5 [103].

$$z = \pm \sqrt{\frac{(1+S_{11})^2 - S_{21}^2}{(1-S_{11})^2 - S_{21}^2}} \tag{4.5}$$

The transmission coefficient expressed in terms of S_{11} and S_{21} in Equation 4.6 [103].

$$t = \frac{S_{21}}{1 - S_{11} \cdot r} \tag{4.6}$$

The real and imaginary parts of refractive index is obtained by implementing Equation 4.2, and real part and imaginary parts are shown in Equations 4.7 and 4.8, respectively [103].

$$p' = \frac{1}{k_0 \cdot d} \cdot (Im[\ln(t)] + 2 \cdot \pi \cdot c) \tag{4.7}$$

$$p'' = \frac{1}{k_0 \cdot d} \cdot Re[\ln(t)] \tag{4.8}$$

where c represents the branch coming from the sin function. p' and p'' is the real and imaginary parts of refractive index, respectively.

The permittivity of the material is obtained from Equation 4.9 in terms of impedance and refractive index [103].

$$\epsilon = \frac{p}{z} \tag{4.9}$$

where ϵ is the permittivity, p is the refractive index, and z is the impedance.

The permeability of a material is presented in Equation 4.10 [103].

$$\mu = p \cdot z \tag{4.10}$$

where μ is the permeability, p is the refractive index, and z is the impedance.

For a structure to be a metamaterial, the real parts of permittivity and permeability should be negative [104]. Figure 4.4 shows the effective permittivity of wide-band metamaterial absorber design. As stated in metamaterial theory, the permittivity of the proposed design is negative. Thus, the proposed design shows metamaterial characteristics. Moreover, the permittivity of the proposed design shows Drude response behavior between 100 THz and 750 THz. Thus, Drude model can be used in the proposed design.
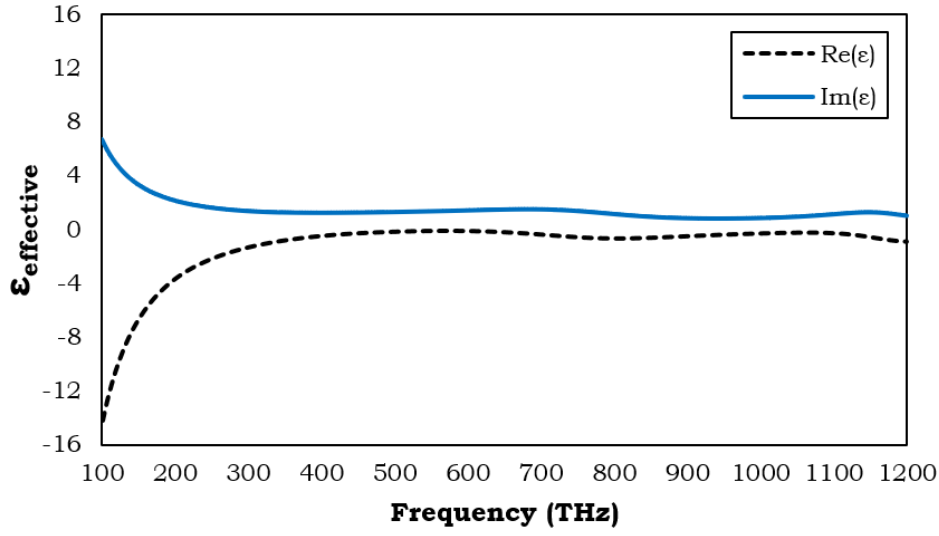
Figure 4.4 S-parameter retrieval results of real (black-dashed line) and imaginary (blue line) parts of effective permittivity

As stated before, real part of permeability should be negative for a structure to be a metamaterial. As seen from Figure 4.5, real part of permeability is negative in two regions (Red-dashed line in Figure 4.5). Hence, the structure is accepted to be a metamaterial. Furthermore, the permeability shows Lorentz response behavior in the studied frequency range.
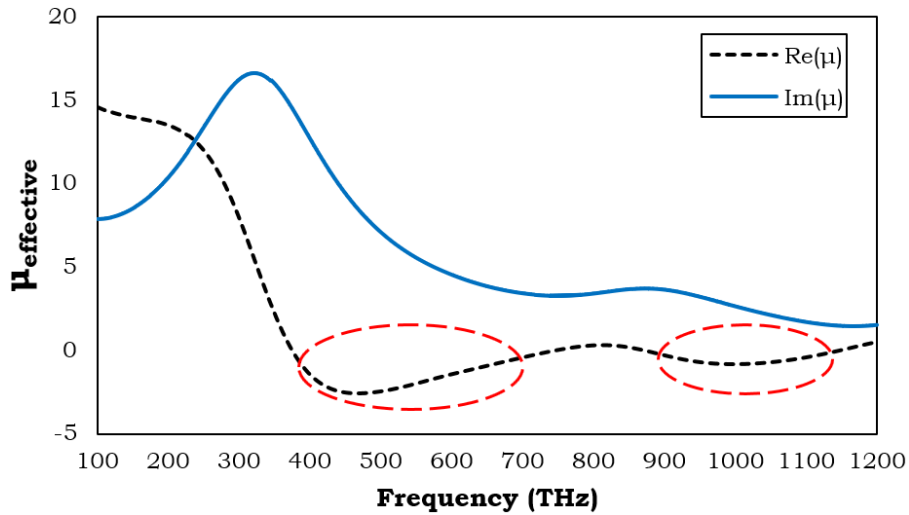
Figure 4.5 S-parameter retrieval results of real (black-dashed line) and imaginary (blue line) parts of effective permeability

According to the results circled (black-dashed circles) in Figure 4.6, real parts of permittivity and permeability are negative which indicates that proposed structure shows left handed characteristics.
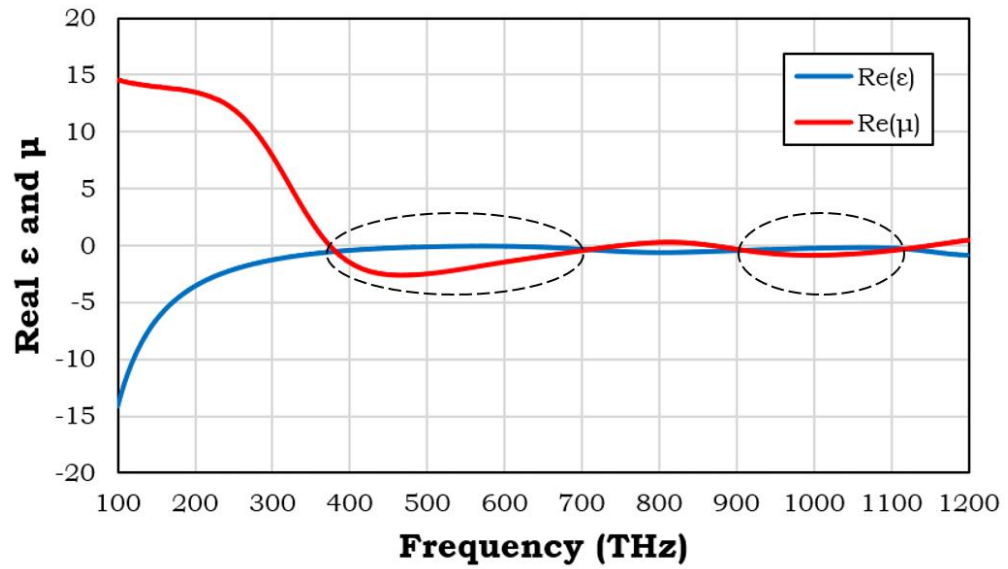
Figure 4.6 Real parts of effective permittivity (blue line) and permeability (red line) with respect to frequency

CHAPTER 5

FIVE-STRIP SI-CNT BASED METAMATERIAL ABSORBER

In this chapter, theory behind the design and results and discussion of the simulated five-strip MTM absorber will be presented and discussed. The absorber designed is presented in detail. Simulations are conducted with and without mechanical loads as explained in the Methodology and Modelling chapter.

5.1 Theory and Design Methodology

The proposed unit cell configuration, which is generated through comprehensive research on established absorber designs including authors' previous work, is shown in Figure 5.1. The unit cell is made of three layers; a square-shaped aluminum plate at the bottom, at the top four rectangular and one square-shaped aluminum resonators, and a square-shaped substrate made of Si-CNT composite sandwiched between aluminum plates. The five resonators are placed on the Si-CNT composite substrate. The dimensions of ground plate and substrate, thickness of substrate, thickness of ground plate, and thickness of resonators are 400 nm, 100 nm, 50 nm, and 20 nm, respectively. After various simulations are carried out, the geometric dimensions are optimized as shown in Table 5.1.

Table 5.1 Geometric dimensions of the five-strip absorber structure

Parameter	w	a	l	y	t	r	x
Value (nm)	50	50	80	100	20	50	400
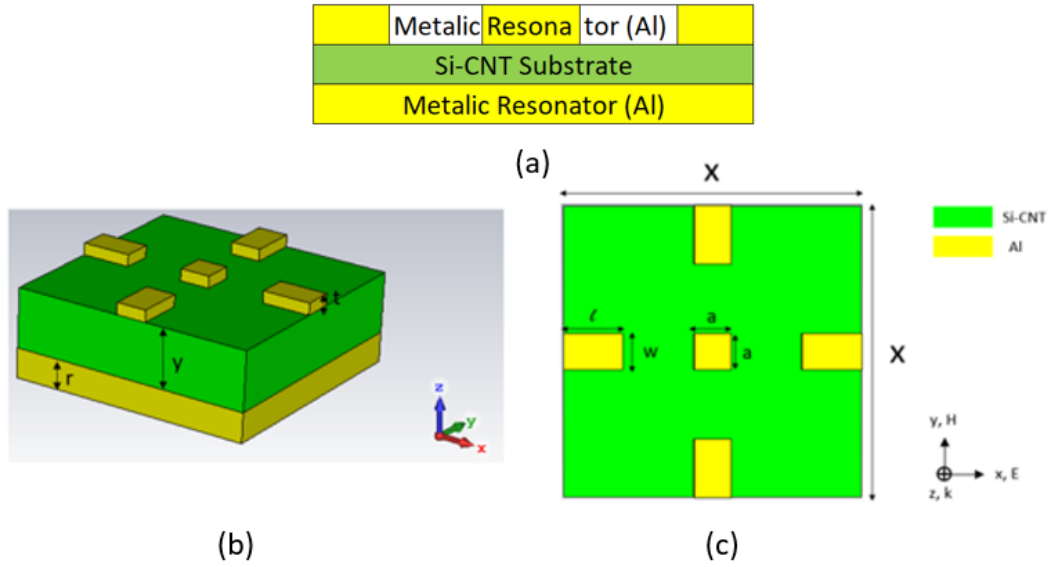
Figure 5.1 Side view (a), isometric view (b), and front view (c) of the five strip MTM structure

5.2 Bending Deformation Mode Methodology

Bending moment is applied in order to analyze the effects of mechanical deformation on absorption and reflection rates. Figure 5.2 shows the concave and convex bends of the proposed MTM absorber. The concave bend is represented with a positive angle, and convex bend is represented with negative angle. All three components of the MTM absorber are bent together in order to obtain the presented shapes in Figure 5.2.
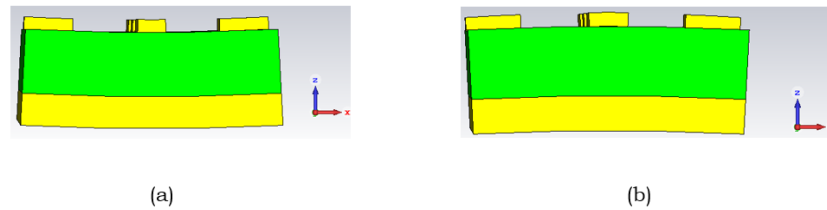
Figure 5.2 (a) 6° bent shape (positive/concave bending), and (b) -6° bent shape (negative/convex bending) of the five-strip MTM absorber

43

Finite Element Modelling (FEM) is done in order to obtain Von Mises stresses and mechanical deformations. Figure 5.3 shows the isometric view of the meshed and colored views of Von Mises stresses and the detailed view of the MTM absorber for the section that maximum Von Mises stresses occurred after bending stress is applied. There are 19450 tetrahedron elements available in this view.

(a)

(b)

(c)
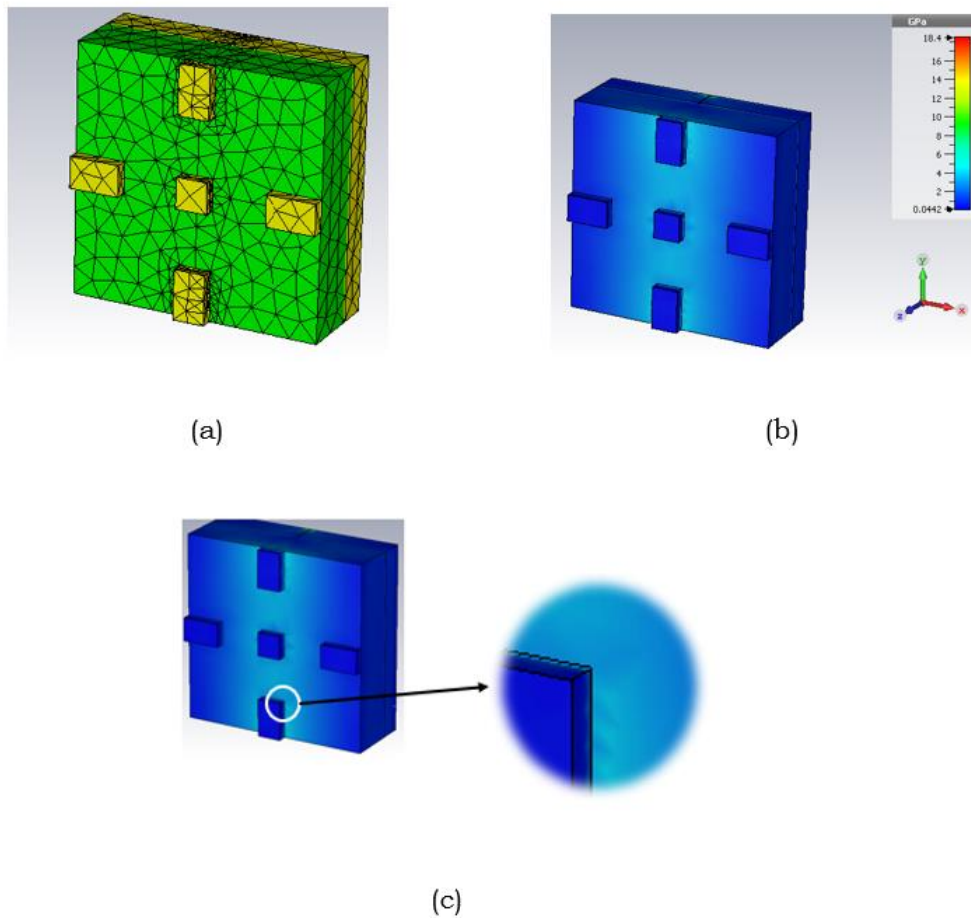
Figure 5.3 Meshed view (a), Von Mises stress view (b) and the place that maximum Von Mises stresses occurred view of the five-strip MTM absorber design (c)

5.3 Simulations without Mechanical Deformation

Separate simulations are done with the pristine models without any mechanical deformation for one, two, three, and four strip resonators in order

to evaluate their absorption rates. Figure 5.4 shows the absorption rates for single, double, triple, and quadruple strips with a middle strip. It is clearly seen from Figure 5.4 that when single resonator is used with middle patch, the absorption rates from 400 THz to 1000 THz clearly lower than the quadruple strip resonator. The increasing strip number increases the absorption rates, so that, the maximum absorption rate achieved with quadruple strip at 943.7 THz (97.97%).
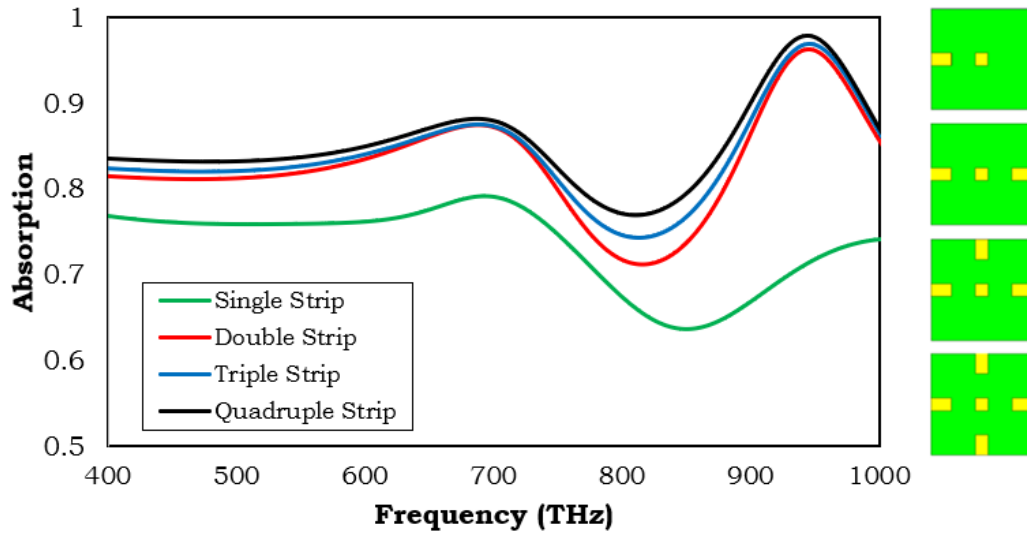
Figure 5.4 Absorption curves of the single, double, triple and quadruple strips with a center patch in the visible and ultraviolet frequency range (400-1000 THz)

The absorption and reflection distribution with respect to frequency is shown in Figure 5.5. The MTM absorber utilizes at least 72% of the sunlight that hits it within the frequency range from 400 THz to 1200 THz. In the visible spectrum (400 THz to 770 THz), the MTM absorber utilizes at least 77% of the sunlight that hits it. There is a single-band absorption response in the visible range. It is located at 686.30 THz, with a rate of 88.24%. The maximum absorption rate is observed as 97.97% in the ultraviolet range at 943.7 THz frequency. Moreover, the mean absorption rate for the visible and ultraviolet frequency range is 83.79%, with a 95% confidence level.

45
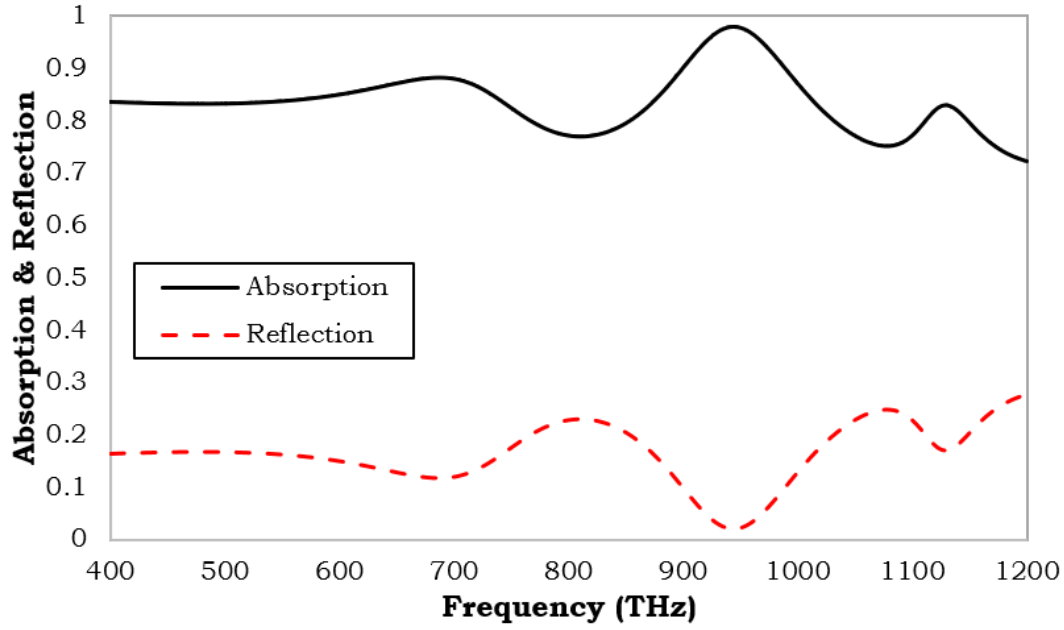
Figure 5.5 Typical absorption and reflectance curves for the five-strip MTM absorber without bending between 400 THz and 1200 THz frequencies

Figure 5.6 shows the simulation results for five-strip MTM absorber according to polarization angles between 10° and 90° with 10° increments under normal incidence radiation. As seen from Figure 5.6, chance in polarization angle does not affect the absorption response of this MTM absorber. The main reason behind this is that the proposed design has symmetric and simple geometry. Hence, variation on polarizations angle do not influence the absorption response of the MTM absorber.
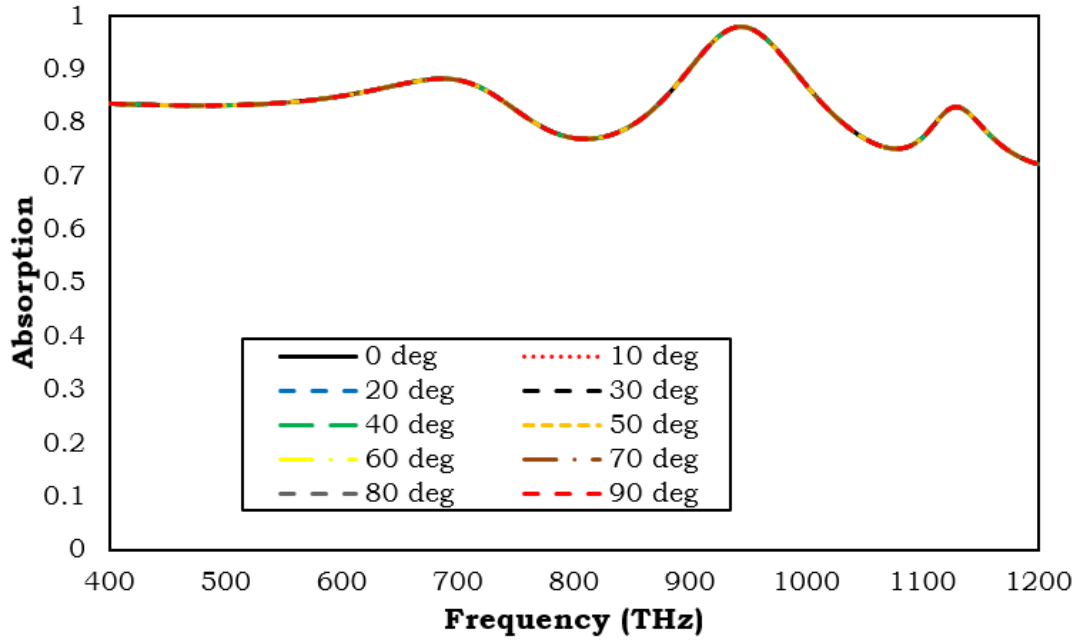
Figure 5.6 Absorption response of the five-strip MTM absorber for polarization angles between 10° and 90° under normal incidence mode of the electromagnetic radiation

5.4 Simulations under Mechanical Load

Simulations of the design and relevant predictions collected are presented in detail in this section.

5.4.1 Mechanical Stresses

Bending stresses are applied in order to analyze the absorption rates of the MTM absorber. Table 5.2 shows bending angles and the resulted maximum von Mises stresses for the five-strip MTM absorber. Positive bending angles cause compression, whereas negative bending angles cause tension on the proposed MTM absorber.

Table 5.2 Bending angle and resulted maximum von mises stress for the five-strip MTM absorber

	Bending Angle	Maximum Stress (GPa)
Concave/Positive Bending	2.00°	1.29
	4.00°	2.59
	6.00°	3.89
	8.00°	5.20
	10.00°	6.53
Convex/Negative Bending	-2.00°	1.29
	-4.00°	2.59
	-6.00°	3.89
	-8.00°	5.20
	-10.00°	6.53

5.4.2 Resonance Shifts with Bending

Resonant frequency shifts occur due to bending stresses applied to the MTM absorber in the ultraviolet range (800 THz to 1050 THz). The response of the MTM absorber is analyzed when the bending angle is varied. The results of this analysis are shown in Figure 5.7. Positive bending angles create compression, while negative bending angles cause tension on the absorber. Positive bending angles (i.e. compression on the absorber) result in positive frequency shifts, and also this operation slightly reduces the absorption rates. On the other hand, negative bending angles (i.e. tension on the absorber) result in negative frequency shifts. Unlike positive bending angles, there is no change in the absorber rates during negative bending. According to the results presented in Figure 5.7, it can be said that by applying bending stresses on proposed MTM absorber, it is possible to have a perfect absorber with different frequency values within the ultraviolet frequency range (800 THz to 1050 THz).
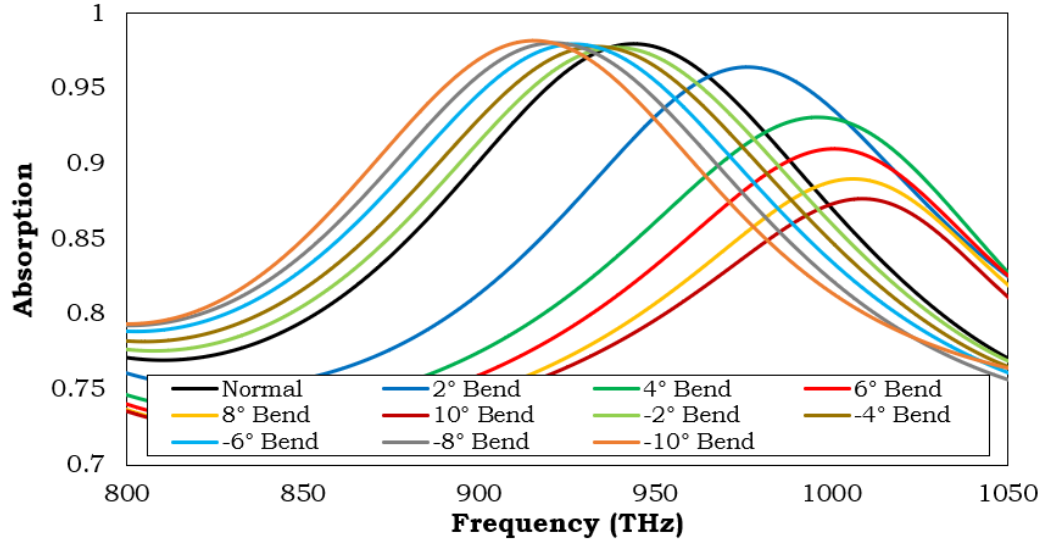
Figure 5.7 Variation of absorption spectra for different bending angles between 800 and 1050 THz

5.4.3 Field Distributions at Resonance Frequency

Changes in electric field, magnetic field, and surface current distribution occur due to bending deformations applied to the absorber. These changes can be on the magnitude or on the direction of the distribution.

Figure 5.8 shows the surface current distribution of the metamaterial absorber at 943.87 THz. This frequency value is obtained from the absorption response of the absorber without applying any bending deformation. As seen from Figure 5.8, bending operation changes the direction of the surface current distribution on the left resonator. The magnitude of the current distribution is also decreased due to bending operations. Concave bend (Figure 5.8-c) decreases the magnitude of the surface current distribution more than convex bend (Figure 5.8-a).

(a)   (b)   (c)
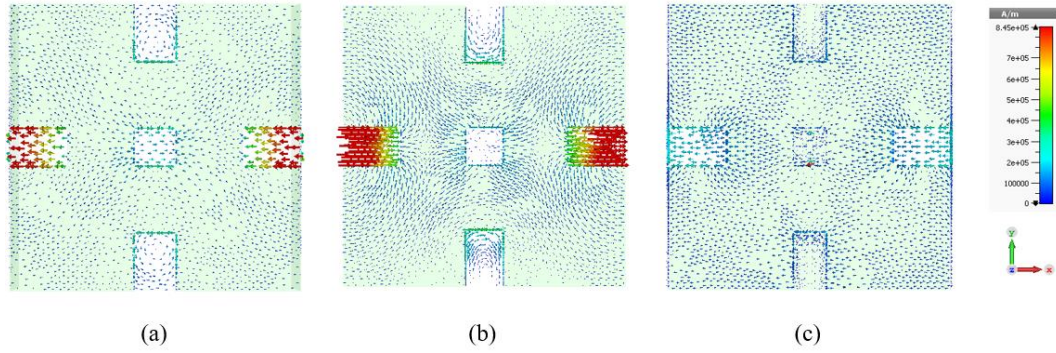
Figure 5.8 Surface current distribution of metamaterial absorber at resonance frequency (943.87 THz) for -6° (a), for 0° (b), and 6° (c) bending angles

Electric field responses of the metamaterial absorber at 943.87 THz with different bending angles are shown in Figure 5.9. Concave bending deformation increases the magnitude of the electric field, while convex bending slightly decreases the magnitude in the center of the absorber.

(a)   (b)   (c)
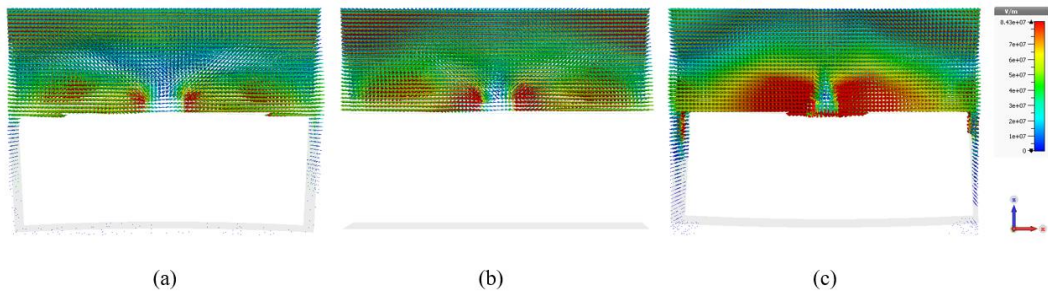
Figure 5.9 Electric-field distribution of metamaterial absorber at resonance frequency (943.87 THz) for -6° (a), for 0° (b), and 6° (c) bending angles

The magnetic field distribution response of the metamaterial absorber is demonstrated in Figure 5.10. Unlike electric field distribution, convex bending increases the magnitude of the magnetic field distribution, whereas concave bending deformations decrease the magnitude throughout the field distribution.
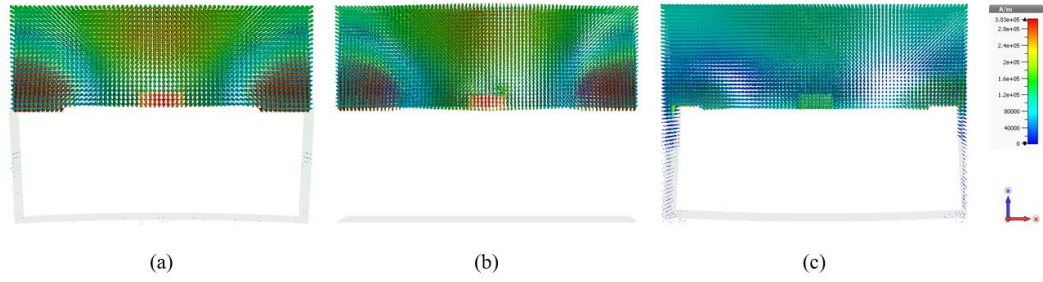
Figure 5.10 Magnetic-field distribution of metamaterial absorber at resonance frequency (943.87 THz) for -6° (a), for 0° (b), and 6° (c) bending angles

5.5 Conclusion

In this chapter, absorber characteristics of a Si-CNT based metamaterial absorber were analyzed within the frequency range from 400 THz to 1200 THz. Simulations were carried out in two parts. In the first part, absorption and reflection characteristics were analyzed without any deformation. The five-strip absorber utilizes at least 72% of the sunlight that hits it. The maximum absorption rate was observed as 97.97% in the ultraviolet range at the frequency of 943.7 THz. Moreover, the mean absorption rate for the visible and ultraviolet frequency range was 83.79% with 95% confidence level. Secondly, mechanical loads in the form of bending moments were applied to the MTM absorber in order to observe the changes in absorption and reflection rates. According to results of this analysis, it can be concluded that resonant frequency shifts can be obtained in ultraviolet range when bending angles are applied for this particular MTM absorber.

CHAPTER 6

SQUARE-STRIP SI-CNT METAMATERIAL ABSORBER

In this chapter, theory and design methodology and results of the simulations that carried out for the square-strip metamaterial absorber are presented. The absorber proposed is presented with all necessary details. Simulations are carried out with and without mechanical loads as explained in Methodology and Modelling chapter.

6.1 Theory and Design Methodology

The proposed unit cell configuration, which is produced in accordance with literature review on recognized absorber designs including authors' previous work, is shown in Figure 6.1. The unit cell made of three layers. A square-shaped aluminum back-plate at the bottom, a Si-CNT composite substrate in the middle, and 8 square-shaped aluminum resonators at the top. 4 small resonators placed in the middle region which are referred as mid-pack, and 4 others are placed on the corners of the Si-CNT substrate absorber. The ground plate is made of a square with 400 nm width and 50 nm thickness. The Si-CNT substrate has a width of 400 nm and a thickness of 100 nm. The mid-pack resonators have a 25 nm width and 20 nm thickness. The corner pack resonators have 100 nm width and 20 nm thickness. Several different geometries and thickness values are used with several simulations in order to determine the geometric dimension that are shown in Table 6.1.

Table 6.1 Geometric dimensions of the square-strip absorber structure

Parameter	v	a	b	c	z	h	x
Value (nm)	20	25	100	50	100	50	400
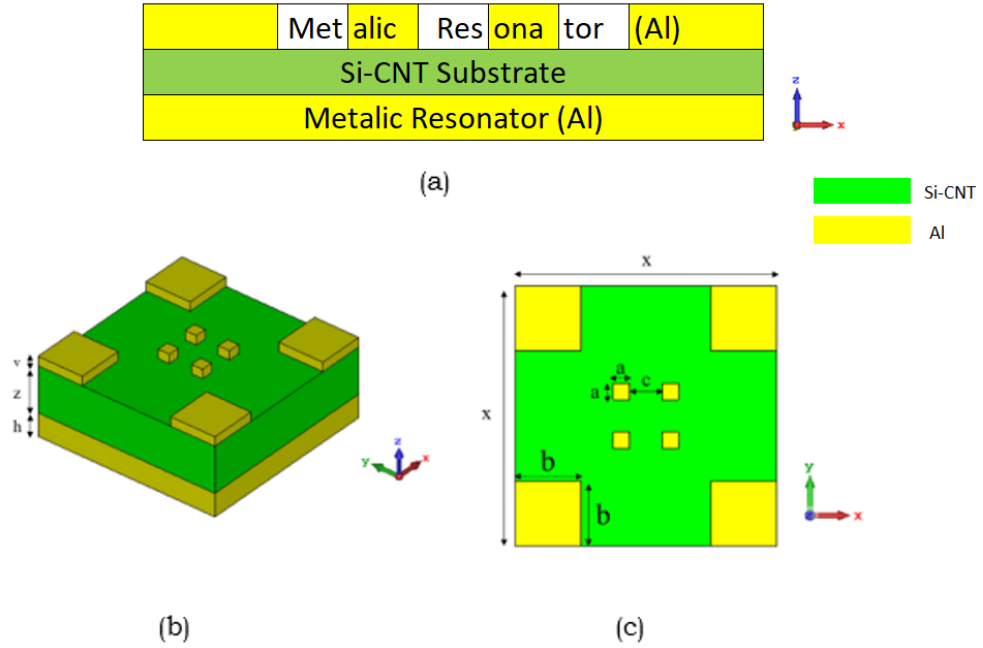
Figure 6.1 Side view (a), isometric view (b), and front view (c) of the square-strip MTM structure

6.2 Bending Deformation Mode Methodology

Bending moment is applied in order to analyze the effects of mechanical deformation on absorption and reflection rates. Figure 6.2 shows the concave and convex bends of the square-strip MTM absorber. The concave bend is represented with a positive angle, and convex bend is represented with negative angle. All three components of the MTM absorber are bent together in order to obtain the presented shapes in Figure 6.2.
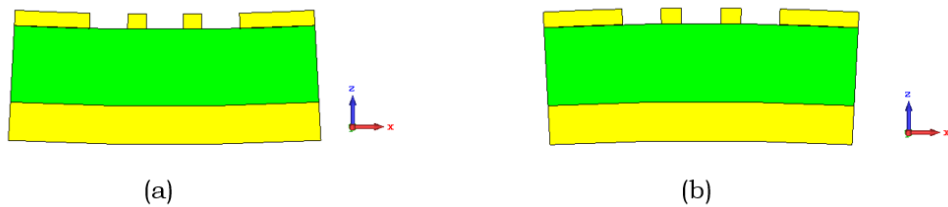
Figure 6.2 (a) 6° bent shape (positive/concave bending), and (b) -6° bent shape (negative/convex bending) of the square-strip MTM absorber

Finite Element Modelling (FEM) is done in order to obtain von Mises stresses and mechanical deformations. Figure 6.3 shows the isometric view of the meshed and colored views of von Mises stresses and the detailed view of the MTM absorber for the section that maximum von Mises stresses occurred after bending stress is applied. There are 19015 tetrahedron elements available in this view.
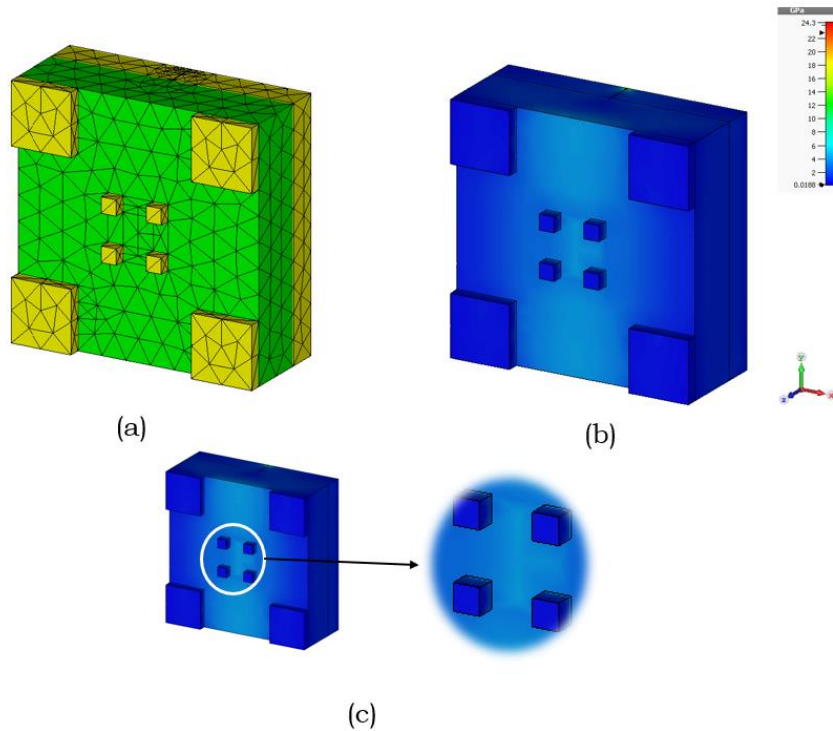
Figure 6.3 Meshed view (a), Von Mises stress view (b) and the place that maximum Von Mises stresses occurred view of the square-strip MTM absorber design (c)

6.3 Simulations without Mechanical Deformation

In order to determine the final shape of the absorber, simulations are carried out for one, two, three, and four-squared geometries with four small square pack in the middle. The simulations are carried out within the visible and ultraviolet frequency range (400 THz – 1200 THz). The results of the simulations are presented in Figure 6.4. The lowest absorption rates are

achieved with one-squared geometry, whereas the highest absorption rates are obtained with four-squared geometry as shown in Figure 6.4.
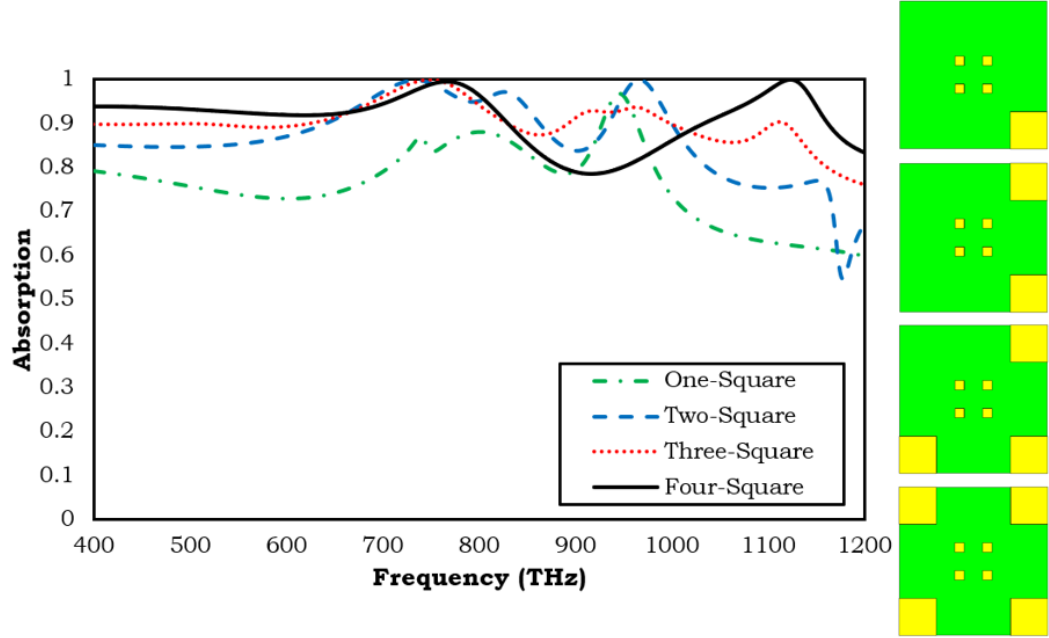
Figure 6.4 Absorption curves of the one, two, three, and four squares with center patch in the visible and ultraviolet frequency range (400-1200 THz)

The absorption and reflection distribution rates with respect to frequency for square-strip MTM absorber is shown in Figure 6.5. By using this MTM absorber, at least 91.84% of the sunlight is absorbed within the visual frequency spectrum (400-770 THz), and the average absorbance is 94.11% within this range. Moreover, the maximum absorption is achieved at 765.5 THz with 99.5%. When ultraviolet frequency spectrum (770 THz – 1200 THz) is considered, maximum absorption rate is 99.96%, and it is located at 1123 THz. The lowest absorption rate is obtained at 916.2 THz with 78.45% within the visible and ultraviolet frequency range. Moreover, the mean absorption rate for the visible and ultraviolet frequency range is 90.67% with a 95% confidence level.
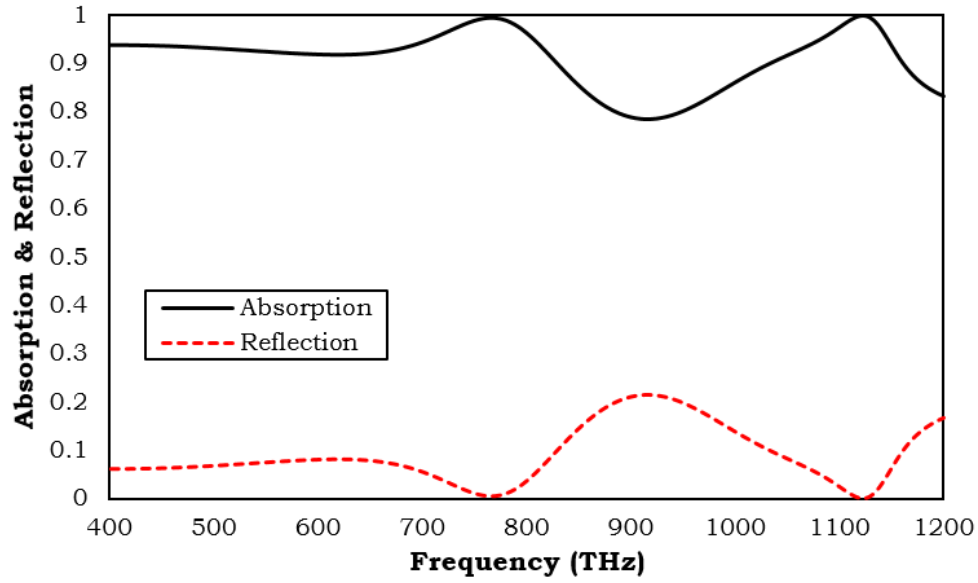
Figure 6.5 Typical absorption and reflectance curves for the square-strip MTM absorber without bending between 400 THz and 1200 THz frequencies

Variation on polarization angle does not affect the absorption response of the MTM absorber. Figure 6.6 shows absorption rates of the absorber with different polarization angles under normal incidence radiation. In order to determine the change in absorption rates, polarization angle is varied between 10° and 90° with 10° intervals. According to results presented in Figure 6.6, variation on polarization angles do not affect the absorption response of this MTM absorber.
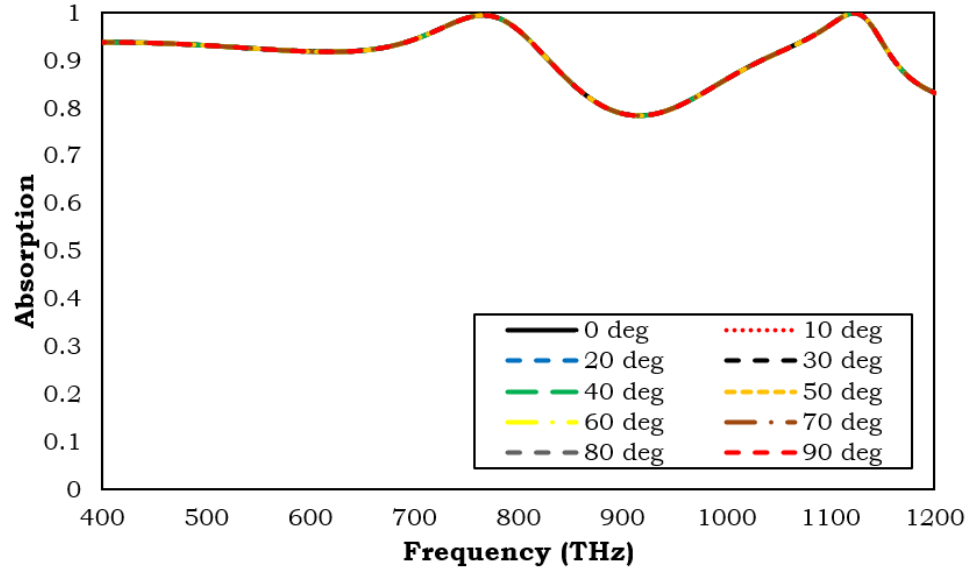
Figure 6.6 Absorption response of the square-strip MTM absorber under normal incidence mode of the electromagnetic radiation with polarization angles between 10° and 90°

6.4 Simulations under Mechanical Load

Simulations of the design and predictions obtained are discussed in detail in this section.

6.4.1 Mechanical Stresses

Bending stresses applied in order to analyze the absorption rates of the MTM absorber. Table 6.2 shows the bending angle and the resulted maximum von Mises stresses for the square-strip MTM absorber. Negative bending angles cause tension, while positive bending angles cause compression on the square-strip MTM absorber, as it is similar to the previously designed MTM absorber.

Table 6.2 Bending angles and resulted maximum von Mises stress for the square-strip MTM absorber

	Bending Angle	Maximum Stress (GPa)
Concave/Positive Bending	2.00°	1.16
	4.00°	2.32
	6.00°	3.49
	8.00°	4.67
	10.00°	5.86
Convex/Negative Bending	-2.00°	1.16
	-4.00°	2.32
	-6.00°	3.49
	-8.00°	4.67
	-10.00°	5.86

6.4.2 Dual-band Absorption with Bending

Figure 6.7 shows the variation of absorption spectra for positive bending angles in 900 THz and 1200 THz frequency range. It is clearly seen that there is a single-band absorption response from the absorber without any bending. The single-band frequency response is located at 1123 THz frequency with a 99.96% absorption rate. This single-band response changes to a nearly perfect dual-band response with 97.98% and 97.01% absorption rates at 1039.4 THz and 1159.3 THz frequencies, after 6° bending applied. There is a slight decrease in the absorption rates due to bending. However, since the reduction is around 3%, it can be neglected.
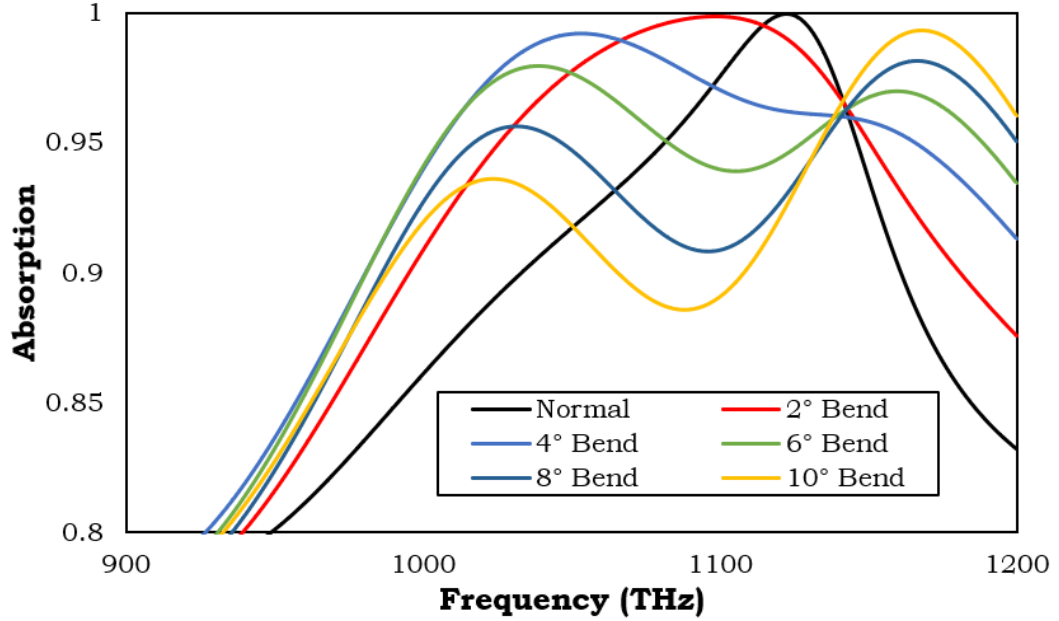
Figure 6.7 Variation of absorption spectra for different positive bending angles between 900 and 1200 THz

6.4.3 Resonance Shifts with Bending

Bending moment on MTM absorber results in negative resonance shifts for this particular MTM absorber within the ultraviolet frequency range (900-1200 THz). With each negative bending angle, there is a slight resonance shift towards left, as seen in Figure 6.8. As mentioned before, tension on the absorber results in negative shifts, as it is the same for this case. The maximum absorption rate is achieved without any bending with 99.96% at 1123 THz. The frequency response of the absorber decreases and shifts towards negative direction while the magnitude of the bending angle is increased in the negative direction. The absorption rates for angles -2°, -4°, -6°, -8°, and -10° have a value between 98.91% and 99.96%. Therefore, since the difference between the maximum and minimum absorption rate is as small as 1%, it can be neglected. To sum up, bending moment causes negative resonance shifts for this MTM absorber.
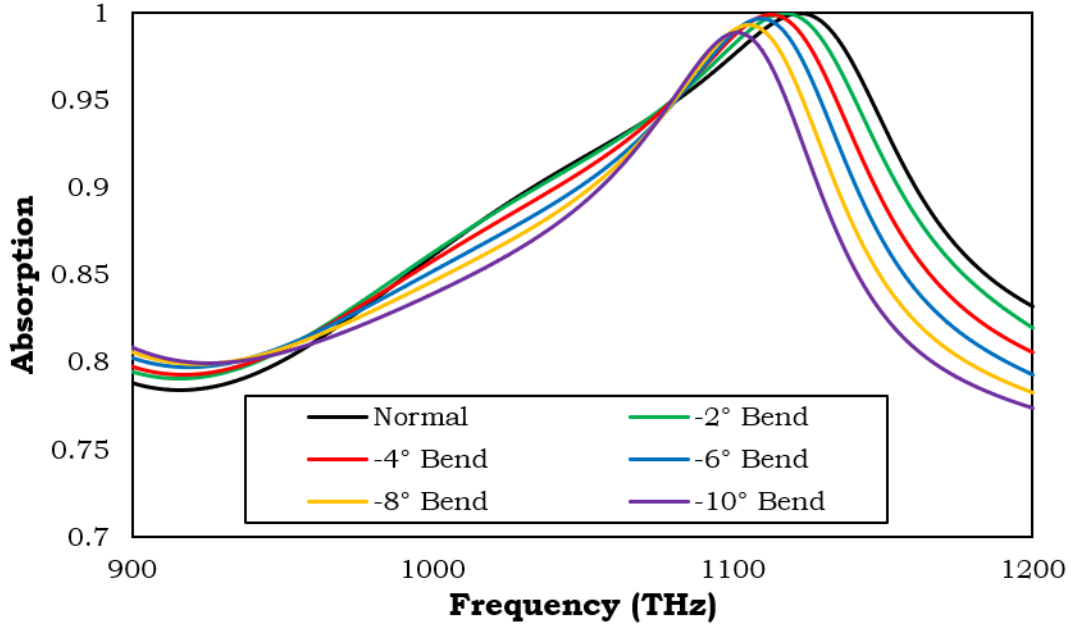
Figure 6.8 Variation of absorption spectra for different negative bending angles between 900 and 1200 THz

6.4.4 Field Distributions at Resonance Frequency

The magnitude and direction of the surface current distribution, electric and magnetic field distributions can change due to bending deformations. These fields are investigated in accordance with the resonance frequency (1122.2 THz) of the proposed metamaterial absorber.

Surface current distributions for 0°, -6°, and 6° bending deformations of the proposed absorber at resonance frequency are presented in Figure 6.9. Surface current distribution concentrate square resonators that placed in each corner. -6° and 0° bending deformations show similar values in the middle. In 6° bending, the magnitude of the surface current is higher when compared with other deformation states.
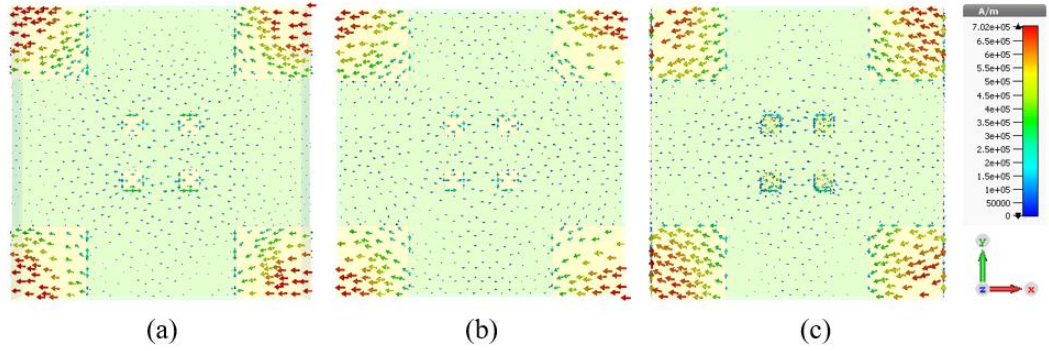
Figure 6.9 Surface current distribution of the square-strip absorber at resonance frequency (1122.2 THz) for -6° (a), for 0° (b), and 6° (c) bending angles

Electric field and magnetic field responses of the proposed absorber for -6°, 0°, and 6° bending deformations are demonstrated in Figures 6.10 and 6.11, respectively. As seen from Figure 6.10, bending deformations reduce electric field for the proposed absorber. The magnitude of magnetic field distribution can increase with convex bending (-6° bending) as seen in Figure 6.11. When both electric and magnetic fields are considered, the contribution of magnetic field is higher that electric field in concave (6° bending) and convex (-6° bending) bending modes.
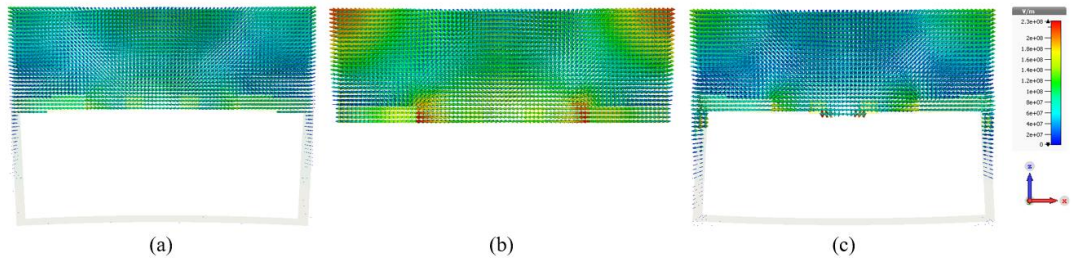
Figure 6.10 Electric-field distribution of metamaterial absorber at resonance frequency (1122.2 THz) for -6° (a), for 0° (b), and 6° (c) bending angles
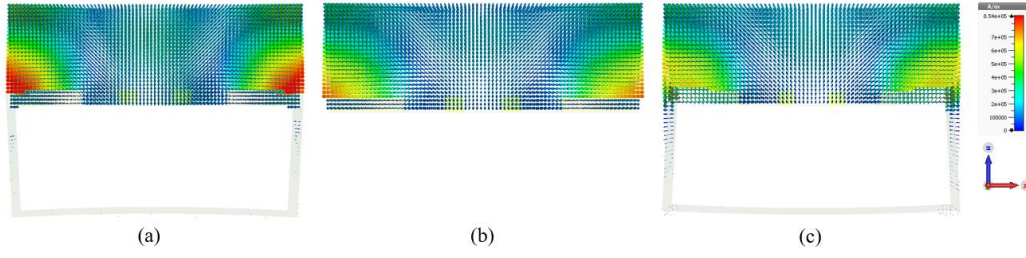
Figure 6.11 Magnetic-field distribution of metamaterial absorber at resonance frequency (1122.2 THz) for -6° (a), for 0° (b), and 6° (c) bending angles

6.5 Conclusion

In this chapter, absorption rates of the square-strip MTM absorber was evaluated in two parts: with and without mechanical bending deformations. In the first part, the MTM absorber was simulated without any bending deformation. According to the simulations done in the first part, the square-strip MTM absorber utilized at least 91.84% of the sunlight that hits it within the visible frequency spectrum (400-700 THz). There was a dual-band frequency response with 99.96% and 99.50% absorption rates in ultraviolet frequency spectrum (700-1200 THz). In the second part, bending moments were applied with different angles that vary between -10° and 10° with 2° increments. Positive/concave bending angles converted the single-band frequency response into dual-band frequency response. On the other hand, negative/convex bending angles result in negative frequency shifts. Finally, surface current, electric and magnetic field distributions were analyzed and presented for the proposed absorber.

CHAPTER 7

WIDE-BAND SI-CNT BASED METAMATERIAL ABSORBER

In this chapter, the design methodology and the theory that is used to generate the wide-band metamaterial absorber is presented and discussed. The simulations are carried out in two separate parts. The first part includes simulations without mechanical load whereas the second part includes simulations under mechanical loads.

7.1 Theory and Design Methodology

The thirdly proposed unit cell has a novel configuration that is based on the literature and authors' previous work. It is presented in Figure 7.1. This unit cell is also made of three layers as the same with the previously proposed absorbers. The first layer is an aluminum ground plate, the second layer is made of Si-CNT composite, and the third layer contains 16 quarter circles and 4 quarter squares. The geometrical dimensions of the absorber are presented in Table 7.1. The substrate and the ground plate have a cross-section with 400 x 400 nm, and a thickness of 100 nm and 50 nm, respectively. In order to determine the dimensions and the geometry shown in Table 7.1, various simulations and trials are performed. As a result of mentioned simulations, the best geometry and dimensions are obtained and presented in Table 7.1.

Table 7.1 Geometric dimensions of the wide-band absorber structure

Parameter	a	r_1	r_2	r_3	r_4	b	t	z	y	x
Value (nm)	10	40	60	80	100	20	50	100	350	400
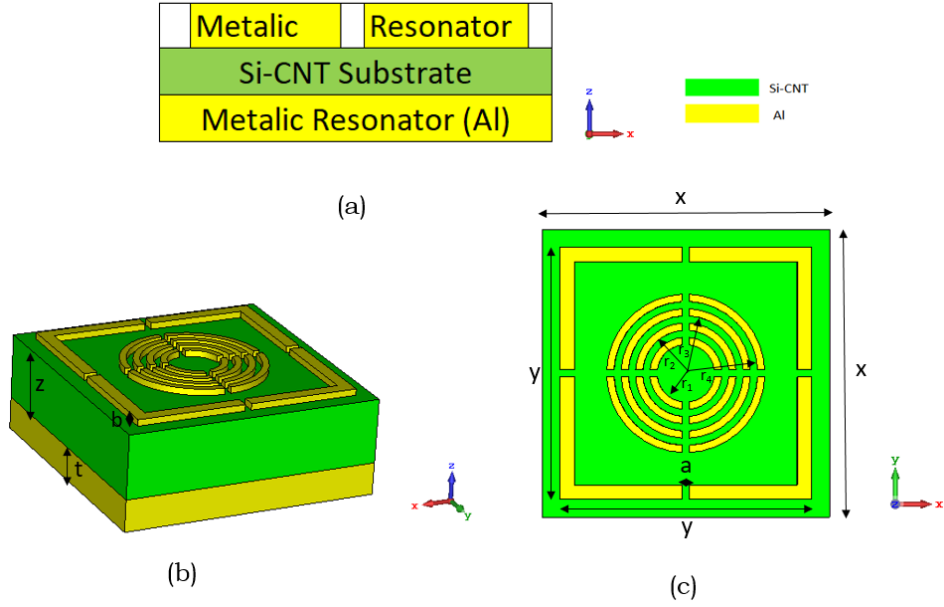
Figure 7.1 Side view (I), isometric view (II), and front view (III) of the wide-band absorber

7.2 Bending Deformation Mode Methodology

As mentioned in the previous designs, absorption and reflection rates for this MTM absorber are examined after bending moment applied with different magnitudes. Concave and convex bend shapes with 6° and -6° angles for this MTM absorber are shown in Figure 7.2. All components of the MTM absorber are bent together for achieving the models in Figure 7.2.
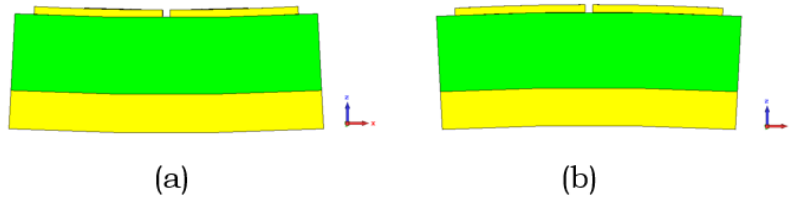
Figure 7.2 (a) 6° bent shape (positive/concave bending), and (b) -6° bent shape (negative/convex bending) of the wide-band MTM absorber

Mechanical bending deformation mode is simulated via Finite Element Method in order to get von Mises stresses and mechanical deformations on

the metamaterial absorber. Meshed, von Mises stresses and the maximum stress views of the absorber are shown in Figure 7.3. In the meshed view, the number of elements are 25264 for 6° bending (See Figure 7.3).
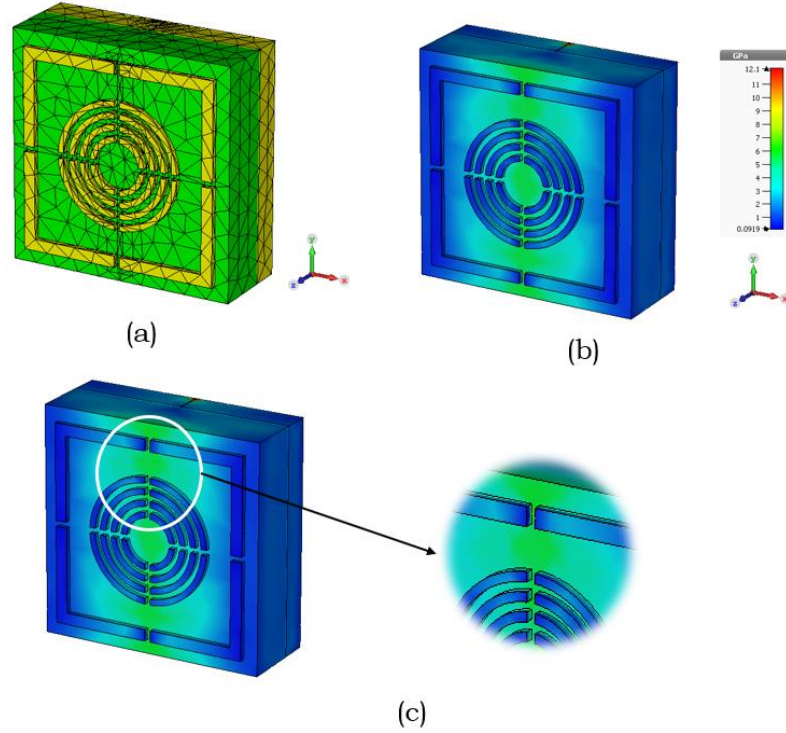
Figure 7.3 Meshed view (a), Von Mises stress view (b) and the place that maximum Von Mises stresses occurred view of the wide-band absorber (c)

7.3 Simulations without Mechanical Deformation

Discrete simulations are carried out in order to determine the number of circles needed to have a better absorption curve. The results of the simulations are shown in Figure 7.4. According to the result obtained from the simulations and presented in Figure 7.4, one, two, and three circled absorbers show lower absorption values when compared to four circled one. In other words, increasing circle number also increases the absorption. Thus, four circled designed is preferred.
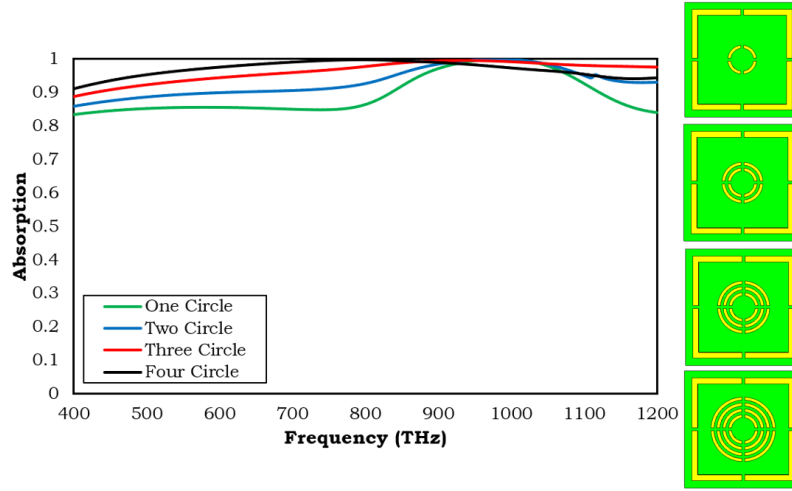
Figure 7.4 Absorption curves of the one, two, three, and four circled simulations of the wide-band absorber in the visible and ultraviolet frequency range (400-1200 THz)

Wide-band absorption response is obtained for the proposed absorber. The absorption and reflection rates are presented in Figure 7.5. At least 91.17% of the electromagnetic energy is absorbed with a corresponding frequency as 400.3 THz. The maximum absorption rate is observed at 794.1 THz with 99.81%. Additionally, 97.10% mean absorption rate is observed for the proposed design with 95% confidence level.
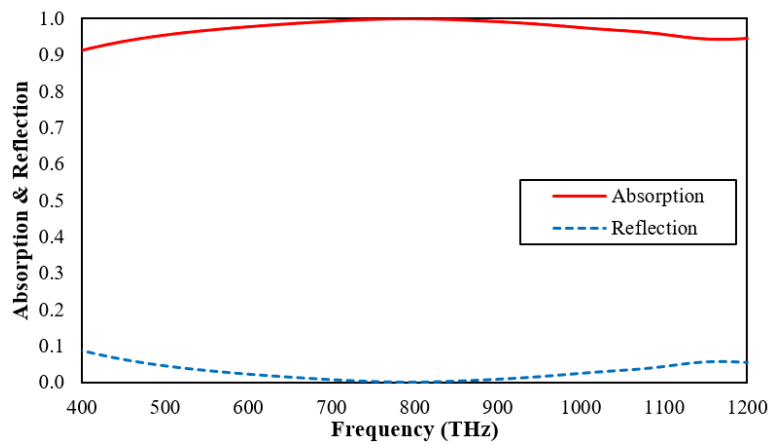
Figure 7.5 Typical absorption and reflectance curves for wide-band absorber without bending between 400 THz and 1200 THz frequencies

Figure 7.6 shows the absorption responses of this MTM absorber for polarization angles between 10° and 90° with 10° increments. Because of having simple geometry and being symmetric, the design shows polarization independent characteristics. Thus, this design can be considered as independent of polarization under normal incidence radiation.
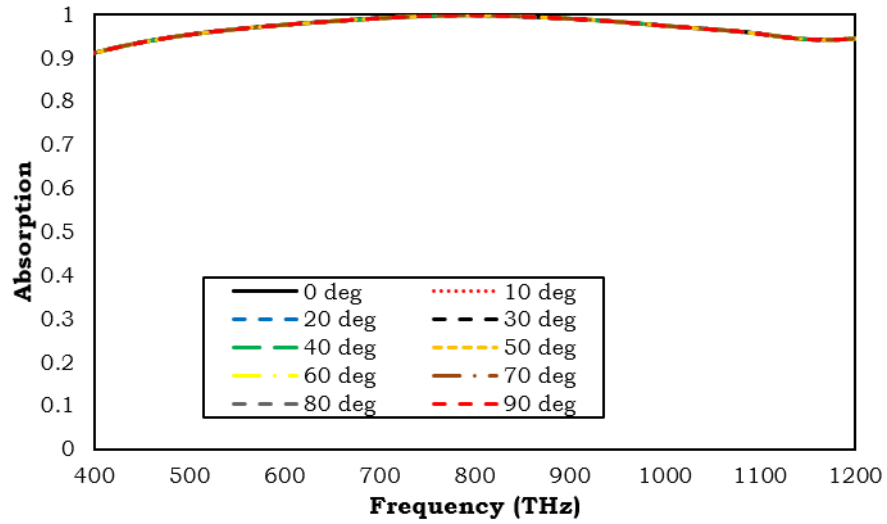
Figure 7.6 Absorption response of the wide-band absorber for different polarization angles under normal incidence mode of the electromagnetic radiation

7.4 Simulations under Mechanical Load

The proposed design simulation results are presented and discussed in detail in this section.

7.4.1 Mechanical Stresses

Mechanical bending moment is applied with different bending angles for analyzing and interpreting the absorption and reflection rates of the MTM absorber. The bending angles and the corresponding von Mises stresses for this MTM absorber are shown in Table 7.2. Convex (negative) bending angles

result in tension on the absorber, whereas concave (positive) bending angles result in compression on the absorber.

Table 7.2 Bending angles and resulted maximum von Mises stress for wide-band absorber

	Bending Angle	Maximum Stress (GPa)
Concave/Positive Bending	2.00°	1.39
	4.00°	2.78
	6.00°	4.18
	8.00°	5.59
	10.00°	7.01
Convex/Negative Bending	-2.00°	1.39
	-4.00°	2.78
	-6.00°	4.18
	-8.00°	5.59
	-10.00°	7.01

7.4.2 Frequency Response of Metamaterial Absorber under Convex Bending

Convex bending slightly increases the absorption rates of this absorber. Figure 7.7 shows the results of the convex bending operation for -2°, -4°, -6°, -8°, and -10° angles. The minimum absorption rate is observed in -2° bending at 400 THz frequency with 91% absorption rate within visible and ultraviolet frequency range (400 THz – 1200 THz). The maximum absorption rate for this analysis is obtained with -10° bending as 99.89% at 764.4 THz frequency. Moreover, the highest absorption rates are achieved with -10° bending in the visible frequency range (400 THz – 770 THz), whereas -2° bending achieved the highest absorption rates within the ultraviolet frequency range (770 THz -1200 THz) as seen in Figure 7.7.
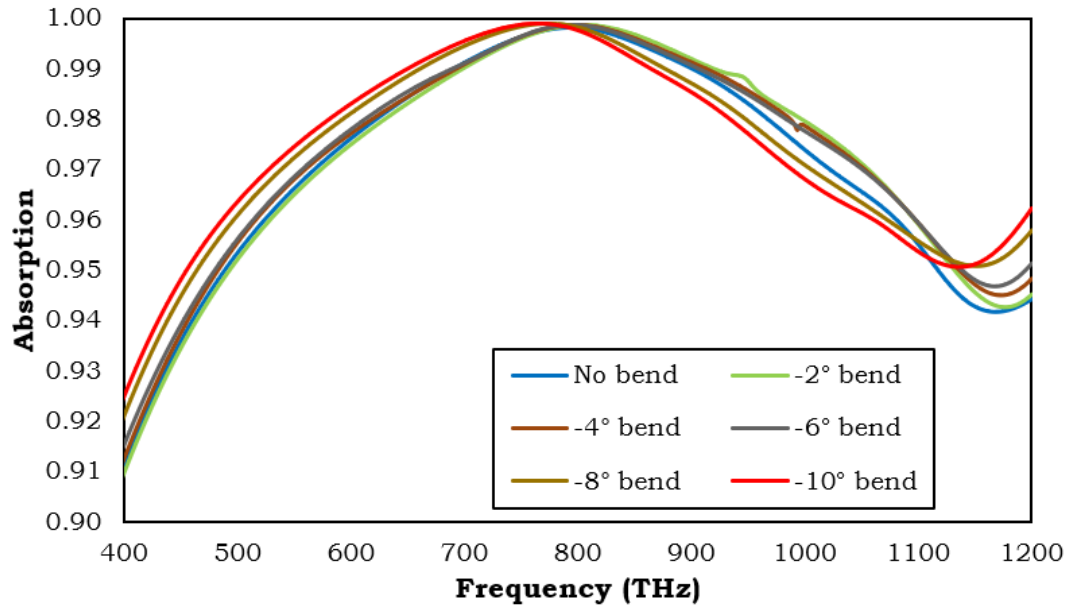
Figure 7.7 Absorption response of the wide-band absorber under convex bending within visible and ultraviolet frequency range (400 THz – 1200 THz)

7.4.3 Absorption Response in Visible Frequency Range under Concave Bending

Figure 7.8 shows the results due to concave bending deformation applied to this absorber for angles 2°, 4°, 6°, 8°, and 10°. In the visible range, highest absorption rates are achieved with 4° bending. Mainly, bending the absorber 4° resulted in increase in absorption rates approximately 5%. Furthermore, the lowest absorption rates are achieved with 10° bending among bending deformations.
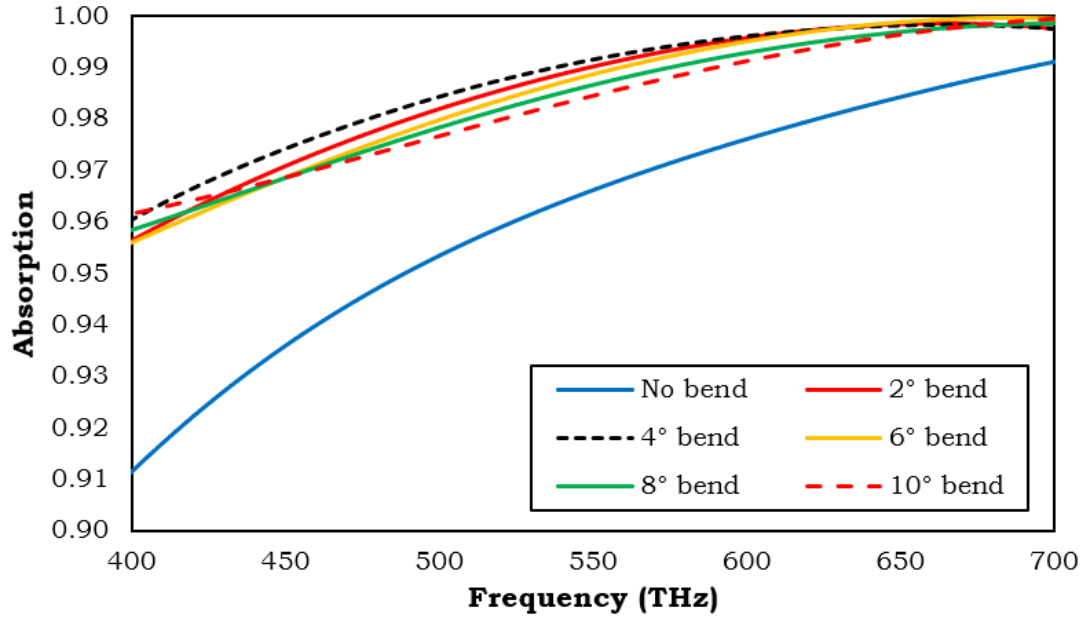
Figure 7.8 Absorption response of the wide-band absorber under concave bending within the visible frequency range (400 THz – 700 THz)

7.4.4 Absorption Response in Ultraviolet Frequency Range Under Concave Bending

Figure 7.9 shows absorption response of the designed metamaterial absorber for concave bending deformations within the ultraviolet frequency range (700 THz – 1200 THz). Positive bending deformations slightly decrease the absorption rates of the absorber in the ultraviolet frequency range. Additionally, 93.31% absorption rate is obtained for the lowest response within the mentioned frequency range for 4° bending deformation at 1126.3 THz.
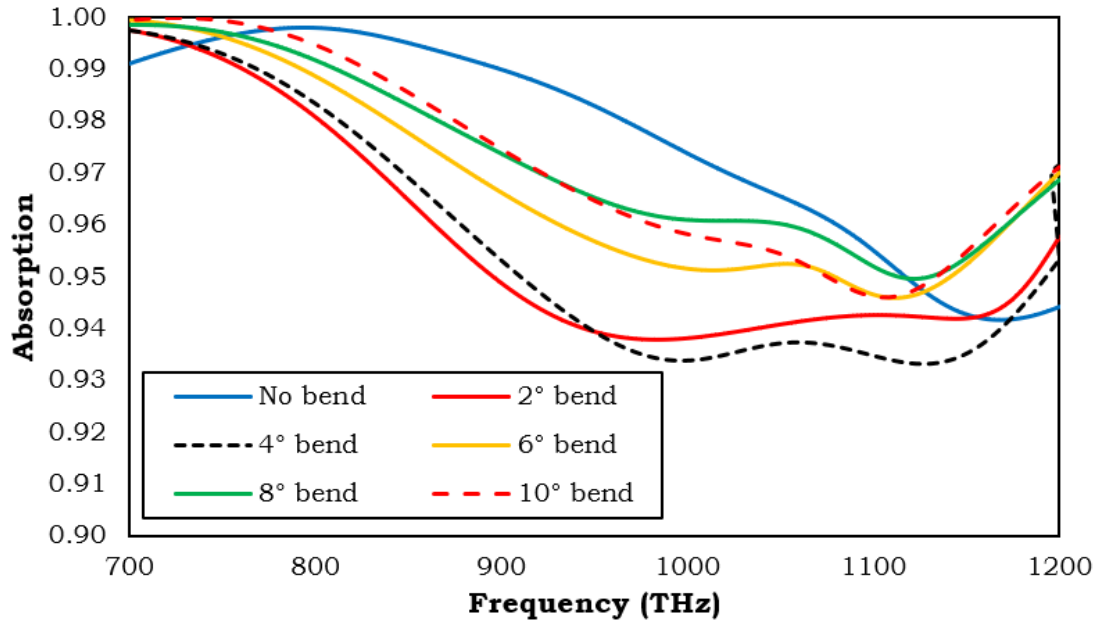
Figure 7.9 Absorption response of the wide-band absorber under concave bending within the ultraviolet frequency range (700 THz – 1200 THz)

Concave (positive bending angles) bending cause frequency shifts for this absorber. Figure 7.10 shows the combination of Figures 7.8 and 7.9 that presents the absorption rates for the wide-band absorber between 400 THz and 1000 THz. Within this frequency range, the maximum absorption peak is obtained in 10° bending (red dashed line in Figure 7.10) at 724.8 THz frequency with 99.99% absorption rate. Moreover, resonance frequency shifts occurred when concave bending is applied to the absorber as seen in Figure 7.10.
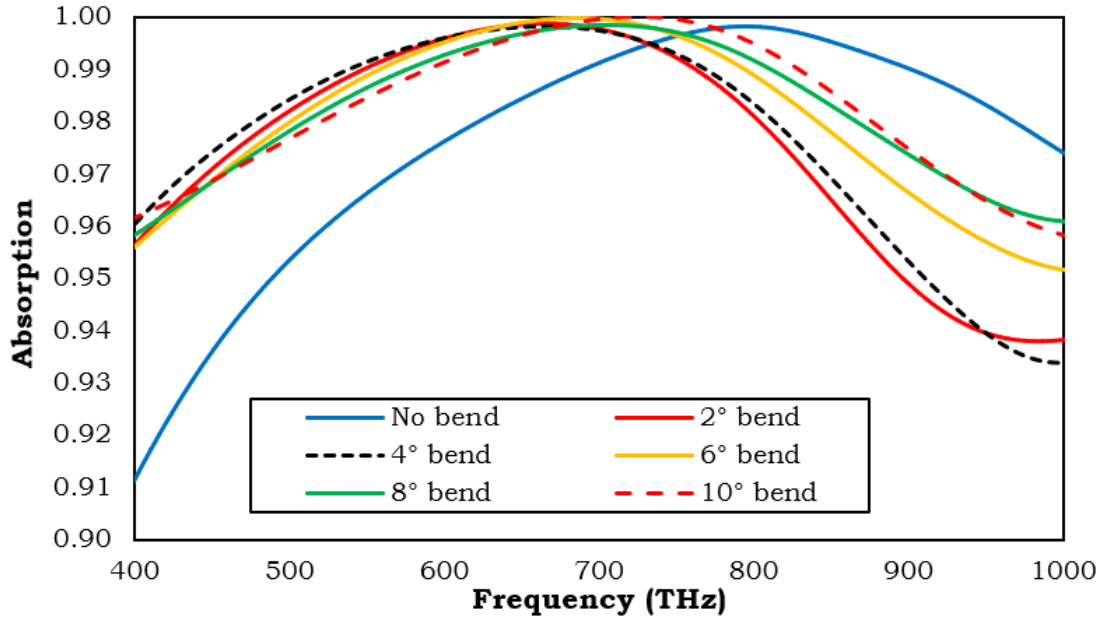
Figure 7.10 Absorption rates of the wide-band absorber under positive bending between 400 THz and 1000 THz frequency range

7.4.5 Field Distributions at Resonance Frequency

During simulations field distributions are monitored. Surface current distribution for -6°, 0°, and 6° bending deformations of the proposed absorber at 796.41 THz is shown in Figure 7.11. 0° bending and -6° bending show similar surface current distribution at 796.41 THz. Hence, both simulations have similar absorption response as shown in Figure 7.7. However, in 6° bending deformation case, the current distribution is high in the middle region of the absorber.
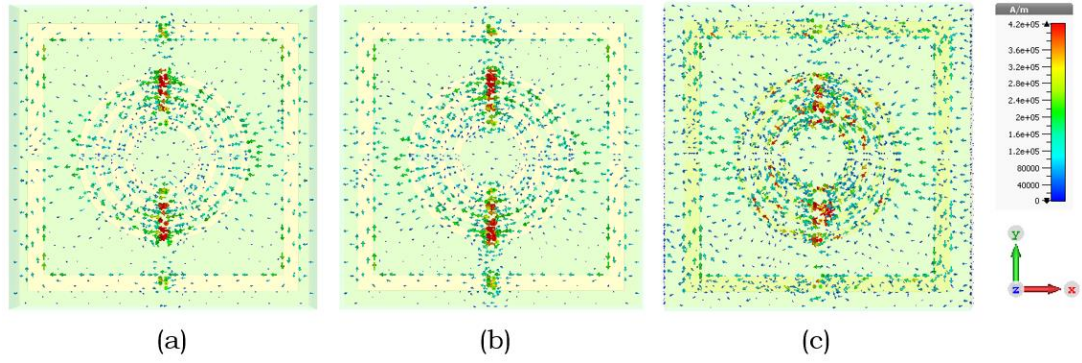
Figure 7.11 Surface current distribution of the proposed absorber at resonance frequency (796.41 THz) for convex (-6°) (a), for 0° (b), and concave (6°) (c) bending modes

Electric-field and magnetic field distributions of the proposed absorber at 796.41 THz are presented in Figure 7.12 and 7.13, respectively. The magnitude of the electric-field distribution seems to be increasing with concave bending whereas convex and 0° bending show similar electric field distribution. The maximum value of electric-field is seen in 6° bending deformation mode in the center of the absorber (See Figure 7.12-c).
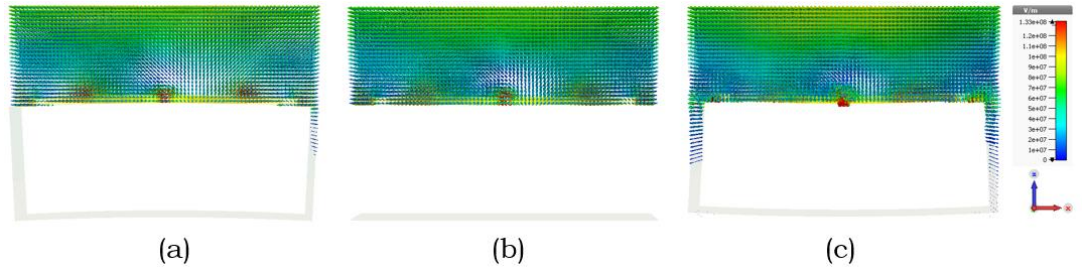
Figure 7.12 Electric-field distribution of the proposed absorber at resonance frequency (796.41 THz) for convex (-6°) (a), for 0° (b), and concave (6°) (c) bending angles

Magnetic field distribution show similar characteristics among three bending modes. However, the magnitude of 6° bending mode is slightly less than others. Higher magnetic field magnitude is observed around the resonators.
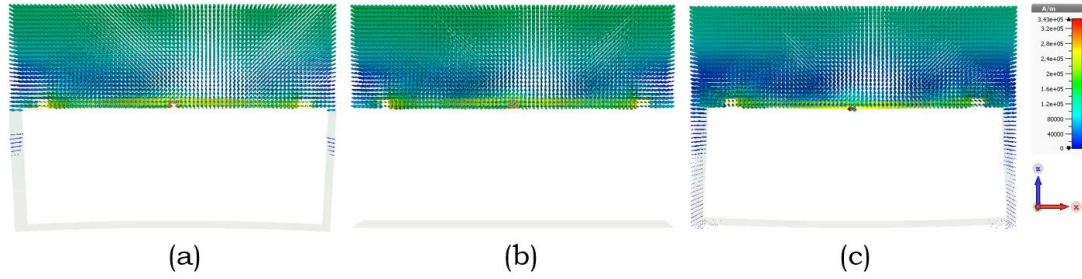
Figure 7.13 Magnetic-field distribution of the proposed absorber at resonance frequency (796.41 THz) for convex (-6°) (a), for 0° (b), and concave (6°) (c) bending angles

7.5 Conclusion

In this chapter, a wide-band metamaterial absorber was proposed. The proposed absorber was simulated in two parts within the frequency range from 400 THz to 1200 THz. In the first part, absorption and reflection characteristics were analysed. Within this context, a wide-band absorption response was observed with a minimum absorption rate as 91.17% at 400.3 THz. At 794.1 THz, the maximum absorption rate was observed with 99.81%. In the second part, concave and convex bending deformations were applied to the proposed absorber with angles that vary between -10° and 10° with 2° increments. The results of the simulations showed that concave bending caused frequency shifts between 600 THz and 800 THz. Absorption rates are slightly decreased within the ultraviolet frequency range (700 – 1200 THz) under concave bending while convex bending resulted in increase in absorption rates. Additionally, the proposed absorber was simulated with different polarization angles and the results showed that the proposed absorber is polarization independent.

CHAPTER 8

CONCLUSIONS

8.1 Conclusion of the Thesis

The main objective of this research is to evaluate the effects of bending deformations on electro-optical properties of three novel Si-CNT based metamaterial absorbers designed to perform in the visible and ultraviolet frequency ranges (400-1200 THz). The metamaterial absorbers are constructed from three layers: ground plate, substrate, and front resonators. The ground plate and front resonators are made of Aluminium metal whereas the substrate is made of Si-CNT composite with 5% CNT. The ground plate and the substrate are the same for all three absorbers. However, the geometry and the quantity of the front resonators are different for all three absorbers.

The simulations are based on Finite Integration Technique and carried out in two parts. In the first part, the absorption and reflection characteristics of the proposed three absorbers are examined without any bending deformation. The results of the simulations show that at least 72%, 91.84%, and 91.17% sunlight is utilized by five-strip, square-strip, and wide-band metamaterial absorbers, respectively.

Secondly, mechanical loads in the form of bending moments are applied to the proposed metamaterial absorbers in order to observe the changes in absorption and reflection rates. According to results of these analyses, it can be concluded that resonant frequency shifts can be obtained in ultraviolet range when bending angles are applied for five-strip metamaterial absorber. Positive bending angles create compression on the substrate, whereas negative ones create tension. Negative resonant frequency shifts are observed when Si-CNT substrate is under tension (i.e. negative bending angles). On the other hand, positive frequency shifts are seen when compressive stresses are applied (i.e. positive bending angles). Moreover, the corresponding absorption rates for resonant frequencies slightly decrease under

75

compression stresses while no change is observed for the tension cases for the five-strip absorber.

Mechanical deformations affect the square-strip metamaterial absorber in two different cases. In the first case, concave bending results in converting a single-band frequency response located at 1123 THz into nearly perfect dual-band response with 97.98% and 97.01% absorption rates. Convex bending deformation mode resulted in negative frequency shifts. The absorption response shifts towards left with each bending angle increment. The absorption rates change between 98.91% and 99.96%. Since the difference is around 1%, it is considered to be negligible.

Concave mechanical bending deformation caused frequency shifts between 600 THz and 800 THz for the wide-band metamaterial absorber. The maximum absorption rate under bending is achieved with 10° bending. Absorption rates are slightly decreased within the ultraviolet frequency range under concave bending, while convex bending results in an increase in absorption rates. The maximum absorption rate is achieved with -10° convex bending.

Finally, three proposed absorbers are simulated with different polarization angles and the results exhibit that they are polarization independent. Additionally, surface current, electric field, and magnetic field distributions of all three metamaterial absorbers are presented and discussed.

According to the results of the simulations, three absorbers are suitable for solar PV applications because they have high absorption rates in the visible frequency range (400 THz – 770 THz). Thus, this study might be feasible in terms of energy generation.

8.2 Future Work

In this thesis, theoretical and numerical analyses are carried out for three metamaterial absorbers. These theoretical applications are investigated

through computer simulations. In order to gain more insight into the limitations of this research study and achieve more accurate results, experimentation shall be conducted as a future work. Moreover, different geometries and different composites can be used to evaluate the impacts of bending stresses on metamaterial absorbers. Furthermore, different and combined mechanical loads, such as tension, compression, and torsion can be applied to the metamaterial absorber in order to see the impacts of different and combined mechanical loadings on the electro-optical properties of metamaterial absorbers. Finally, cost analysis is suggested to be performed for each absorber.

REFERENCES

[1] T. L. Frölicher and F. Joos, "Reversible and irreversible impacts of greenhouse gas emissions in multi-century projections with the NCAR global coupled carbon cycle-climate model," *Clim. Dyn.*, vol. 35, no. 7, pp. 1439–1459, 2010.

[2] S. Jain, "The current and future perspectives of biofuels," in *Biomass, Biopolymer-Based Materials, and Bioenergy: Construction, Biomedical, and other Industrial Applications*, Elsevier, 2019, pp. 495–517.

[3] R. F. Davis, "Polyvinyl Fluoride Films for Photovoltaic Modules," in *Polyvinyl Fluoride: Technology and Applications of PVF*, Elsevier Inc., 2012, pp. 317–328.

[4] C. J. Cleveland and C. Morris, "Photovoltaics," in *Handbook of Energy*, Elsevier, 2014, pp. 287–302.

[5] A. Chipouline, S. Sugavanam, V. A. Fedotov, and A. E. Nikolaenko, "THz bandwidth optical switching with carbon nanotube metamaterial," *J. Opt. (United Kingdom)*, vol. 14, no. 11, p. 153902, 2012.

[6] C. Ferrara and D. Philipp, "Why do PV modules fail?," *Energy Procedia*, vol. 15, no. 2011, pp. 379–387, 2012.

[7] D. E. Carlson *et al.*, "Corrosion Effects in Thin-Film Photovoltaic Modules," *Prog. Photovoltaics Res. Appl.*, vol. 11, no. 6, pp. 377–386, 2003.

[8] F. Bilotti and L. Sevgi, "Metamaterials: Definitions, properties, applications, and FDTD-based modeling and simulation," *International Journal of RF and Microwave Computer-Aided Engineering*, vol. 22, no. 4. Wiley Periodicals, Inc, pp. 422–438, 2012.

[9]   M. Lobet, B. Majérus, and P. Lambin, "Graphene on epsilon-near-zero metamaterials as perfect electromagnetic absorber," in *Carbon-Based Nanoelectromagnetics*, Elsevier, 2019, pp. 169–189.

[10] G. Singh and A. Marwaha, "A Review of Metamaterials and its Applications," *Int. J. Eng. Trends Technol.*, vol. 19, no. 6, pp. 305–310, 2015.

[11] J. Sun and N. M. Litchinitser, "Metamaterials," in *Fundamentals and Applications of Nanophotonics*, Elsevier Inc., 2016, pp. 253–307.

[12] D. L. Jaggard, A. R. Mickelson, and C. H. Papas, "On electromagnetic waves in chiral media," *Appl. Phys.*, vol. 18, no. 2, pp. 211–216, 1979.

[13] Mikhail A. Noginov, Nikolay I. Zheludev, Allan D. Boardman, and Nader Engheta, "Metamaterials: Fundamentals and Applications II," 2009.

[14] M. Obaidullah, "Single-Walled Carbon Nanotube Based Metamaterial Absorber for Solar Cell Application," Middle East Technical University NCC, 2017.

[15] M. Obaidullah, V. Esat, and C. Sabah, "Single- and multi-walled carbon nanotubes for solar cell applications," *Int. J. Mod. Phys. B*, vol. 32, no. 21, p. 1830007, 2018.

[16] S. Kar and P. K. Tewari, "Nanotechnology for domestic water purification," in *Nanotechnology in Eco-Efficient Construction: Materials, Processes and Applications*, Elsevier Ltd, 2013, pp. 364–427.

[17] A. M. Holban, A. M. Grumezescu, and E. Andronescu, "Inorganic nanoarchitectonics designed for drug delivery and anti-infective surfaces," in *Surface Chemistry of Nanobiomaterials: Applications of Nanobiomaterials*, Elsevier Science Ltd., 2016, pp. 301–327.

[18] P. J. F. Harris, "Carbon nanotube composites," *Int. Mater. Rev.*, vol. 49,

no. 1, pp. 31–43, 2004.

[19]   S. Iijima and T. Ichihashi, "Single-shell carbon naotubes of 1-nm diameter," *Lett. to Nat.*, vol. 363, pp. 603–605, 1993.

[20]   S. Reich, C. Thomsen, and J. Maultzsch, *Carbon Nanotubes: Basic Concepts and Physical Properties*. 2007.

[21]   D. V. M. F. L., T. S. H., B. R. H., and H. A. J., "Carbon Nanotubes: Present and Future Commercial Applications," *Science (80-.).*, vol. 339, no. February, p. 535, 2013.

[22]   F. C. Campbell, "Introduction to Composite Materials," in *Structural Composite Materials*, ASM International, 2010, pp. 1–5.

[23]   A. K. Kaw, *Mechanics of Composite Materials*, 2nd ed. Taylor & Francis, 2006.

[24]   D. K. Y. Tam, S. Ruan, P. Gao, and T. Yu, "High-performance ballistic protection using polymer nanocomposites," in *Advances in Military Textiles and Personal Equipment*, 2012, pp. 213–237.

[25]   D. R. Askeland, P. P. Fulay, and W. J. Wright, *The Science and Engineering of Materials*, 6th ed. 2010.

[26]   E. Kymakis and G. A. J. Amaratunga, "Single-wall carbon nanotube/conjugated polymer photovoltaic devices," *Appl. Phys. Lett*, vol. 80, p. 112, 2002.

[27]   E. Fortunato *et al.*, "Optoelectronic Devices from Bacterial NanoCellulose," in *Bacterial Nanocellulose: From Biotechnology to Bio-Economy*, Elsevier Inc., 2016, pp. 179–197.

[28]   R. G. Budynas and J. K. Nisbett, *Shigley's Mechanical Engineering Design*, 9th ed. McGraw-Hill, 2011.

[29] E. C. Garnett, M. L. Brongersma, Y. Cui, and M. D. McGehee, "Nanowire Solar Cells," *Annu. Rev. Mater. Res.*, vol. 41, no. 1, pp. 269–295, 2011.

[30] "Infrastructure definition and meaning | Collins English Dictionary." .

[31] L. Sapling and L. Macmillan, "EM Spectrum - Chempendix," 2018. [Online]. Available: https://sites.google.com/site/chempendix/em-spectrum. [Accessed: 14-Dec-2019].

[32] A. Jäger-Waldau, "European Commission PV Status Report 2017," 2017.

[33] Sharp, "A Century of Sincerity and Creativity," 2017.

[34] M. A. Green, "Silicon photovoltaic modules: A brief history of the first 50 years," *Progress in Photovoltaics: Research and Applications*, vol. 13, no. 5. pp. 447–455, 2005.

[35] D. M. Bagnall and M. Boreland, "Photovoltaic technologies," *Energy Policy*, vol. 36, no. 12, pp. 4390–4396, Dec. 2008.

[36] "Global solar cell production 2019, Statista." [Online]. Available: https://www.statista.com/statistics/278917/global-solar-cell-production/. [Accessed: 19-Sep-2020].

[37] J. N. Roy, *Solar Photovoltaic Technology Production*. Springer, 2018.

[38] L. El Chaar, L. A. Lamont, and N. El Zein, "Review of photovoltaic technologies," *Renew. Sustain. Energy Rev.*, vol. 15, no. 5, pp. 2165–2175, 2011.

[39] T. K. Manna and S. M. Mahajan, "Nanotechnology in the development of photovoltaic cells," *2007 Int. Conf. Clean Electr. Power, ICCEP '07*, pp. 379–386, 2007.

[40] E. Van Kerschaver and G. Beaucarne, "Back-contact solar cells: A review," *Prog. Photovoltaics Res. Appl.*, vol. 14, no. 2, pp. 107–123, 2006.

[41] S. Kajari-Schröder, I. Kunze, and M. Köntges, "Criticality of cracks in PV modules," *Energy Procedia*, vol. 27, pp. 658–663, 2012.

[42] A. M. Gabor *et al.*, "Soldering induced damage to thin Si solar cells and detection of cracked cells in modules," *21st Eur. Photovolt. Sol. Energy Conf. Dresden, Ger. Sept*, no. January 2006, pp. 4–8, 2006.

[43] S. T. Hsu and T. C. Wu, "Simulated Wind Action on Photovoltaic Module by Non-uniform Dynamic Mechanical Load and Mean Extended Wind Load," in *Energy Procedia*, 2017, vol. 130, pp. 94–101.

[44] R. M. Gul, H. Ahsan, F. Ullah, and M. S. Rehan, "Mechanical Testing and Failure Analysis of Photovoltaic Modules," 2016, vol. 2016, no. Eesd.

[45] R. Mickiewicz *et al.*, "Effect of Encapsulation Modulus on the Response of PV Modules to Mechanical Stress," *26th Eur. Photovolt. Sol. Energy Conf.*, pp. 3157–3161, 2011.

[46] T. Zhang *et al.*, "Experimental and theoretical research on bending behavior of photovoltaic panels with a special boundary condition," *Energies*, vol. 11, no. 12, 2018.

[47] S. Suzuki, T. Doi, A. Masuda, and T. Tanahashi, "Bending cyclic load test for crystalline silicon photovoltaic modules," *Jpn. J. Appl. Phys.*, vol. 57, no. 2, 2018.

[48] N. I. Landy, S. Sajuyigbe, J. J. Mock, D. R. Smith, and W. J. Padilla, "Perfect metamaterial absorber," *Phys. Rev. Lett.*, vol. 100, no. 20, 2008.

[49] S. Ghosh, S. Bhattacharyya, and K. V. Srivastava, "Bandwidth-Enhancement of an Ultrathin Polarization Insensitive Metamaterial Absorber," *Microw. Opt. Technol. Lett.*, vol. 56, no. 3, pp. 350–355, 2014.

[50] W. Ma, Y. Wen, and X. Yu, "Theoretical and experimental demonstrations of a dual-band metamaterial absorber at mid-infrared," *IEEE Photonics Technol. Lett.*, vol. 26, no. 19, pp. 1940–1943, 2014.

[51] B. X. Wang, X. Zhai, G. Z. Wang, W. Q. Huang, and L. L. Wang, "Design of a Four-Band and Polarization-Insensitive Terahertz Metamaterial Absorber," *IEEE Photonics J.*, vol. 7, no. 1, pp. 1–8, Feb. 2015.

[52] S. Ghosh, S. Bhattacharyya, D. Chaurasiya, and K. V. Srivastava, "An ultrawideband ultrathin metamaterial absorber based on circular split rings," *IEEE Antennas Wirel. Propag. Lett.*, vol. 14, pp. 1172–1175, 2015.

[53] P. Rufangura and C. Sabah, "Dual-band perfect metamaterial absorber for solar cell applications," *Vacuum*, vol. 120, pp. 68–74, Oct. 2015.

[54] J. Kaur, S. Punia, T. Pathak, M. Kataria, and K. Kumar, "Role of biosensors in environmental monitoring," in *Modern Approaches to Environmental Biotechnology*, 2016, pp. 195–208.

[55] W. Xu, L. Xie, and Y. Ying, "Mechanisms and applications of terahertz metamaterial sensing: A review," *Nanoscale*, vol. 9, no. 37, pp. 13864–13878, Oct. 2017.

[56] M. Obaidullah, V. Esat, and C. Sabah, "Thin film (6,5) semiconducting single-walled carbon nanotube metamaterial absorber for photovoltaic applications," *Opt. Eng.*, vol. 56, no. 12, p. 1, Dec. 2017.

[57] B. Mulla and C. Sabah, "Perfect metamaterial absorber design for solar cell applications," *Waves in Random and Complex Media*, vol. 25, no. 3,

pp. 382–392, Jul. 2015.

[58]   G. Hashmi, M. H. Imtiaz, and S. Rafique, "Towards High Efficiency Solar Cells : Composite Metamaterials," *Glob. J. Res. Eng. Electr. Electron. Eng.*, vol. 13, no. 10, 2013.

[59]   A. K. Geim and K. S. Novoselov, "The rise of graphene," *Nat. Mater.*, vol. 6, no. 3, pp. 183–191, Mar. 2007.

[60]   P. Karfa, S. De, K. C. Majhi, R. Madhuri, and P. K. Sharma, "Functionalization of carbon nanostructures," *Compr. Nanosci. Nanotechnol.*, vol. 1–5, pp. 123–144, 2019.

[61]   G. Centi and S. Perathoner, "Carbon Nanotubes for Sustainable Energy Applications," *ChemSusChem*, vol. 4, no. 7, pp. 913–925, 2011.

[62]   P. J. F. Harris, *Carbon nanotube science: Synthesis, properties and applications*, vol. 9780521828. Cambridge University Press, 2009.

[63]   J. Stejskal, "Polymers of Phenylenediamines," *Prog. Polym. Sci.*, vol. 41, no. C, pp. 1–31, Feb. 2015.

[64]   B. Wu, F. Zhuo, F. Long, W. Gu, Y. Qing, and Y. Liu, "A management strategy for solar panel battery super capacitor hybrid energy system in solar car," in *8th International Conference on Power Electronics - ECCE Asia: "Green World with Power Electronics", ICPE 2011-ECCE Asia*, 2011, pp. 1682–1687.

[65]   H. Qiao and Q. Wei, "Functional nanofibers in lithium-ion batteries," in *Functional Nanofibers and their Applications*, Elsevier, 2012, pp. 197–208.

[66]   B. J. Landi, M. J. Ganter, C. D. Cress, R. A. DiLeo, and R. P. Raffaelle, "Carbon nanotubes for lithium ion batteries," *Energy Environ. Sci.*, vol. 2, no. 6, pp. 638–654, Jun. 2009.

[67] J. Yan, M. J. Uddin, T. J. Dickens, and O. I. Okoli, "Carbon nanotubes (CNTs) enrich the solar cells," *Sol. Energy*, vol. 96, pp. 239–252, Oct. 2013.

[68] J. Wei *et al.*, "Double-walled carbon nanotube solar cells," *Nano Lett.*, vol. 7, no. 8, pp. 2317–2321, Aug. 2007.

[69] X. Liu, M. Wang, S. Zhang, and B. Pan, "Application potential of carbon nanotubes in water treatment: A review," *J. Environ. Sci. (China)*, vol. 25, no. 7, pp. 1263–1280, Jul. 2013.

[70] P. Rufangura and C. Sabah, "Polarization angle insensitive dual-band perfect metamaterial absorber for solar cell applications," *Phys. Status Solidi Curr. Top. Solid State Phys.*, vol. 12, no. 9–11, pp. 1241–1245, 2015.

[71] A. Faruk and C. Sabah, "Terahertz metamaterial absorber comprised of H-shaped resonator within split-square ring and its sensory application," *Optik (Stuttg).*, vol. 192, p. 162976, Sep. 2019.

[72] J. Hofer, Z. Nagy, and A. Schlueter, "Electrical Design and Layout Optimization of Flexible Thin-Film Photovoltaic Modules," *EU PVSEC 2016 Proc.*, no. February 2017, pp. 2481–2485, 2016.

[73] P. Sharma, S. P. Duttagupta, and V. Agarwal, "A novel approach for maximum power tracking from curved thin-film solar photovoltaic arrays under changing environmental conditions," in *IEEE Transactions on Industry Applications*, 2014, vol. 50, no. 6, pp. 4142–4151.

[74] N. A. Vinnichenko, A. V. Uvarov, I. A. Znamenskaya, H. Ay, and T. H. Wang, "Solar car aerodynamic design for optimal cooling and high efficiency," *Sol. Energy*, vol. 103, pp. 183–190, May 2014.

[75] F. Umer, M. S. Aslam, M. S. Rabbani, M. J. Hanif, N. Naeem, and M. T.

Abbas, "Design and optimization of solar carport canopies for maximum power generation and efficiency at Bahawalpur," *Int. J. Photoenergy*, vol. 2019, 2019.

[76] B. Abbasipour, B. Niroumand, and S. M. Monir Vaghefi, "Compocasting of A356-CNT composite," *Trans. Nonferrous Met. Soc. China (English Ed.*, vol. 20, no. 9, pp. 1561–1566, Sep. 2010.

[77] H. Belyadi, E. Fathi, and F. Belyadi, "Hydraulic Fracturing in Unconventional Reservoirs," in *Hydraulic Fracturing in Unconventional Reservoirs*, 2019, pp. 215–231.

[78] D. R. H. Jones and M. F. Ashby, "Engineering Materials 1," in *Engineering Materials 1*, 2nd ed., 2019, pp. 31–47.

[79] P. S. Liu and G. F. Chen, "Characterization Methods," in *Porous Materials*, Elsevier, 2014, pp. 493–532.

[80] James G. Speight, *Unconventional Gas Production*, no. 2. 2019.

[81] H. Chen *et al.*, "Thermal conductivity of polymer-based composites: Fundamentals and applications," *Prog. Polym. Sci.*, vol. 59, pp. 41–85, Aug. 2016.

[82] P. Scallan, "Material evaluation and process selection," in *Process Planning*, Butterworth-Heinemann, 2003, pp. 109–170.

[83] R. Pal, *Electromagnetic, mechanical, and transport properties of composite materials*, vol. 158. CRC Press, 2014.

[84] A. Shrivastava, "Plastic Properties and Testing," in *Introduction to Plastics Engineering*, Elsevier, 2018, pp. 49–110.

[85] J. J. Sheng, "Steam Flooding," in *Enhanced Oil Recovery Field Case Studies*, Elsevier Inc., 2013, pp. 361–388.

[86] D. M. Liu, W. H. Tuan, and C. C. Chiu, "Thermal diffusivity, heat capacity and thermal conductivity in Al2O3Ni composite," *Mater. Sci. Eng. B,* vol. 31, no. 3, pp. 287–291, 1995.

[87] R.-M. Wang, S.-R. Zheng, and Y.-P. Zheng, "Other properties of polymer composites," in *Polymer Matrix Composites and Technology*, Elsevier, 2011, pp. 513–548.

[88] L. Dubrovinsky, "Thermal Expansion and Equation of State," in *Encyclopedia of Materials: Science and Technology*, Elsevier, 2002, pp. 1–4.

[89] M. N. Velea and S. Lache, "Thermal Expansion of Composite Laminates," *Bull. Transilv. Univ. Braşov •*, vol. 8, no. 57, 2015.

[90] Z. Wang *et al.*, "Mechanical behavior of Al-based matrix composites reinforced with Mg58Cu28.5Gd11Ag2.5 metallic glasses," *Adv. Powder Technol.*, vol. 25, no. 2, pp. 635–639, 2013.

[91] K. Kaneto, M. Tsuruta, G. Sakai, W. Y. Cho, and Y. Ando, "Electrical conductivities of multi-wall carbon nano tubes," *Synth. Met.*, vol. 103, no. 1–3, pp. 2543–2546, 1999.

[92] "Physical and Mechanical Properties of Silicon." [Online]. Available: https://www.azooptics.com/Article.aspx?ArticleID=254. [Accessed: 15-Feb-2020].

[93] G. Liu *et al.*, "Highly Dense and Perfectly Aligned Single-Walled Carbon Nanotubes Fabricated by Diamond Wire Drawing Dies," vol. 17, p. 36, 2019.

[94] "Silicon - High Precision Machining." [Online]. Available: https://www.insaco.com/materials/other-materials/silicon. [Accessed: 21-Apr-2020].

[95]   S. Jibran, Muhammad, Zuberi, "Computational Modelling of Carbon Nanotube Reinforced Polymer Composites," Middle East Technical University NCC, 2014.

[96]   E. Pop, D. Mann, Q. Wang, K. Goodson, and H. Dai, "Thermal Conductance of an Individual Single-Wall Carbon Nanotube above Room Temperature."

[97]   "Silicon (Si) Semiconductors." [Online]. Available: https://www.azom.com/article.aspx?ArticleID=8346. [Accessed: 15-Feb-2020].

[98]   Z. Nan, C. Wei, Q. Yang, and Z. Tan, "Thermodynamic Properties of Carbon Nanotubes."

[99]   L. Deng *et al.*, "Coefficient of thermal expansion of carbon nanotubes measured by Raman spectroscopy," *Cit. Appl. Phys. Lett*, vol. 104, p. 51907, 2014.

[100]   J. M. Wernik and S. A. Meguid, "Atomistic-based continuum modeling of the nonlinear behavior of carbon nanotubes," *Acta Mech.*, vol. 212, no. 1–2, pp. 167–179, 2010.

[101]   Y. V. Milman, I. V. Gridneva, and A. A. Golubenko, "Construction of stess-strain curves for brittle materials by indentation in a wide temperature range," *Sci. Sinter.*, vol. 39, no. 1, pp. 67–75, 2007.

[102]   X. Shen *et al.*, "Triple-band terahertz metamaterial absorber: Design, experiment, and physical interpretation," *Appl. Phys. Lett.*, vol. 101, no. 15, p. 154102, Oct. 2012.

[103]   A. Faruk, "Design and Analysis of Sub-THZ Metamaterial Structures for Absorber, Sensor, and Switch Applications," Middle East Technical University NCC, 2019.

[104] C. Sabah, "Tunable metamaterial design composed of triangular split ring resonator and wire strip for S-and C-microwave bands," *Prog. Electromagn. Res. B*, vol. 22, no. 22, pp. 341–357, 2010.